JBC ARTICLE

A distinct talin2 structure directs isoform specificity in cell adhesion

Received for publication, August 30, 2019, and in revised form, June 23, 2020 Published, Papers in Press, June 30, 2020, DOI 10.1074/jbc.RA119.010789

Erumbi S. Rangarajan[1], **Marina C. Primi**[1], **Lesley A. Colgan**[2], **Krishna Chinthalapudi**[1], **Ryohei Yasuda**[2], **and Tina Izard**[1,*]

From the [1]*Cell Adhesion Laboratory, Department of Integrative Structural and Computational Biology, The Scripps Research Institute, Jupiter, Florida, USA and* [2]*Neuronal Signal Transduction, Max Planck Florida Institute for Neuroscience, Jupiter, Florida, USA*

Edited by Mike Shipston

Integrin receptors regulate normal cellular processes such as signaling, cell migration, adhesion to the extracellular matrix, and leukocyte function. Talin recruitment to the membrane is necessary for its binding to and activation of integrin. Vertebrates have two highly conserved talin homologs that differ in their expression patterns. The F1–F3 FERM subdomains of cytoskeletal proteins resemble a cloverleaf, but in talin1, its F1 subdomain and additional F0 subdomain align more linearly with its F2 and F3 subdomains. Here, we present the talin2 crystal structure, revealing that its F0-F1 di-subdomain displays another unprecedented constellation, whereby the F0-F1-F2 adopts a new cloverleaf-like arrangement. Using multiangle light scattering (MALS), fluorescence lifetime imaging (FLIM), and FRET analyses, we found that substituting the corresponding residues in talin2 that abolish lipid binding in talin1 disrupt the binding of talin to the membrane, focal adhesion formation, and cell spreading. Our results provide the molecular details of the functions of specific talin isoforms in cell adhesion.

Talin plays pivotal roles in integrin activation as well as in cell migration, invasion, and cancer metastasis (1–4). Talin activates integrin by binding to the β cytoplasmic integrin tail domain (4, 5), which controls focal adhesion dynamics and invadopodium formation (6–9), and thus invasion (7, 10–12). Talin is crucial for initial mechanical force generation (13, 14) and is also involved in calpain-induced focal adhesion disassembly (6, 8). Furthermore, talin binds to and activates phosphatidylinositol phosphate kinase γ, which then generates phosphatidylinositol 4,5-bisphosphate (PIP_2) that controls focal adhesion dynamics (15–19). Talin is further involved in recruiting moesin in complex with the sodium-hydrogen antiporter 1 (NHE-1) that regulates the pH at invadopodia, thereby providing stability to the generation of the invadopodium and the matrix (7).

Talin is a ∼270-kDa cytoskeletal protein characterized by an N-terminal globular head domain (residues 1–400) and a C-terminal tail domain (residues 437–2,541) that are connected by a linker that contains a calpain-II cleavage site (20, 21). The talin head domain comprises a four point one, ezrin, radixin, moesin (FERM) domain that binds to the talin C-terminal domain and to the cytoplasmic integrin β tail domain (5). The talin tail domain harbors 13 single amphipathic α-helical vinculin-binding sites (22–32) as well as two actin-binding sites (33–35) in addition to the F-actin–binding site that is located on the F2 and F3 subdomains of the FERM domain (33–37).

Vertebrates have two highly conserved isoforms with ∼76% sequence identity, but they are not functionally redundant. We know a lot about the talin1 structure and function, whereas much less has been published on talin2 both in terms of structure and function. Talin1 is ubiquitously expressed, whereas talin2 is primarily found in the heart, brain, and skeletal muscle (38, 39). Talin1 is also expressed at smaller focal adhesions in the peripheral region, whereas talin2 is mainly found at large focal adhesions and fibrillar adhesions (40, 41). Upon phosphorylation by Cdk5, talin1 controls focal adhesion dynamics, integrin activation, cell migration, invasion, and metastasis (2, 3), whereas talin2 controls focal adhesion assembly and focal adhesion kinase signaling in cells that are depleted of talin1 (14).

Talin1 knockout mice are embryonic lethal by E8.5–E9.0 due to gastrulation defects (42). *Talin2* knockout mice display mild skeletal myopathy at 3 months of age resulting from defects in the myotendinous junction (43). Talin2 can fully rescue the profound defects in focal adhesions and the organization of the cytoskeleton that are manifest in *talin1*-null cells (44). Thus, talin1 and talin2 seemed at first glance to be functionally redundant. However, the two isoforms transduce mechanical force differently. Under tension, talin1 recruits vinculin, but with talin2, vinculin recruitment occurs even in the absence of its F-actin–binding domain (45). Further, cardiac myocyte talin2 is necessary for proper integrin β1D expression, whereas talin1 can preserve heart function in the absence of talin2. Loss of both talin isoforms from the heart muscle results in myocyte instability and dilated cardiomyopathy (46).

Cell migration and invasion is inhibited by an antibody therapeutic that down-regulates talin2 by targeting human epidermal growth factor 2 for cancer treatment (47). However, depletion of talin2 has no effects on integrin β1 activation (3). A recent *talin2*-null study on T-cell exosomes showed reduced binding of integrins αLβ2 and α4β7 to the intercellular adhesion molecule-1 (ICAM-1) and to the mucosal vascular addressin cell adhesion molecule-1 (MAdCAM-1) (48). Collectively,

---

This article contains supporting information.

* For correspondence: Tina Izard, cmorrow@scripps.edu.

Present address for Krishna Chinthalapudi: Dept. of Physiology and Cell Biology, College of Medicine, Ohio State University, Columbus, Ohio, USA.

Table 1

X-ray data reduction statistics for our human talin2 structure (residues 1–403)

Values for the last shell are shown in parentheses.

Parameters	Values
Space group	$P\,6_5$
Unit cell dimensions	
a, b, c (Å)	58.89, 58.89, 203.8
α, β, γ (degrees)	90, 90, 120
Resolution (Å)	101.9–2.56 (2.60–2.56)
Total measurements	13,1041 (11,611)
No. of unique reflections	12,969 (631)
Wavelength	1.0 Å
R_{pim}[a]	0.044 (0.381)
Signal/noise $I/\sigma(I)$	15.7 (2.7)
Completeness	1.0 (1.0)
Multiplicity	10.1 (5.7)
$CC_{1/2}$[b]	0.998 (0.734)

[a] R_{pim} is the precision-indicating merging R-factor given as $R_{\mathrm{pim}} = \frac{\sum_{hkl}\sqrt{\frac{1}{n-1}}\sum_i |I_{hkl,i} - I_{hkl}|}{\sum_{hkl}\sum_i I_{hkl,i}}$.

[b] $CC_{1/2}$ is a Pearson's correlation coefficient calculated between the average intensities of each random half of measurements of unique reflections.

Table 2

Crystallographic refinement statistics for our human talin2 structure (residues 1–403)

Values for the last shell are shown in parentheses.

Parameters	Values
Resolution (Å)	51.00–2.56 (2.80–2.56)
No. of reflections, working set	12,256
No. of reflections, test set	648
R-factor[a]	0.197 (0.300)
R-free (5% of reflections omitted)	0.246 (0.353)
No. of nonhydrogen atoms	
Protein	3,193
Solvent	117
Average B-factor	
Protein (Å^2)	61.39
Solvent (Å^2)	54.08
Root mean square deviation from ideal values	
Bond lengths (Å)	0.05
Bond angles (degrees)	0.745
Ramachandran favored (%)	96.90
Ramachandran allowed (%)	3.10
Ramachandran outliers	None

[a] $R\text{-factor} = \frac{\sum_{hkl}|F_{\mathrm{obs}}(hkl) - F_{\mathrm{calc}}(hkl)|}{\sum_{hkl} F_{\mathrm{obs}}(hkl)}$.

the talin isoforms do not compensate for the loss of the other, and their functions are distinct.

To determine the molecular basis for the difference between the talin isoform functions, we solved the crystal structure of the talin2 head domain (residues 1–403) to 2.56 Å resolution and provide structural and functional insights into the talin isoforms. Despite their ~76% sequence identity and ~88% sequence similarity for mammalian isoforms, in talin2, whereas the F0-F1 and F2-F3 domains resemble those seen in talin1, F1 engages in distinct interdomain interactions with F2 to result in a completely distinct head domain constellation that has not been observed for any other FERM domain–containing protein. Our solution studies obtained from size-exclusion chromatography support these findings.

Despite their distinct head domain constellation, the mammalian talin isoforms share the same membrane-binding sites. Both full-length proteins are monomeric as determined by multiangle light scattering. This previously disputed observation is now also confirmed by the cryo-EM structure (49) that was published while this manuscript was in revision.

Our confocal microscopy and *in vivo* fluorescence lifetime imaging microscopy (FLIM) with FRET analyses revealed the functional relevance of the talin interaction with the cell membrane. Collectively, we provide significant new insights into talin structure and function that pave the way toward a better understanding of the regulation of integrin function and of fundamental processes in cell biology including the cytoskeletal organization.

Results

Talin2 has an unprecedented FERM constellation

To provide structural insights into the functional differences between the two talin isoforms, we determined the crystal structure of human talin2 (residues 1–403) to 2.56 Å resolution (Tables 1 and 2). Whereas the individual talin2 di-subdomains F0-F1 and F2-F3 are almost identical as seen in the talin1 structure, the F0-F1 motif is rotated by ~140° in talin2 relative to its orientation in talin1 (Fig. 1*A* and Fig. S1). This is accomplished by isoform-specific F1-F2 interdomain interactions.

We assessed the contribution of crystal contacts in the distinct constellations of the F0-F1 di-domain relative to the F2-F3 di-domains in the two talin isoforms (Figs. S2 and S3 and Tables 3 and 4). Murine talin1 crystallized in $P\,2_12_12_1$ as a chimera of residues 1–138 fused to 169–400, whereas our human talin2 (residues 1–403) structure crystallized in space group $P\,6_5$. The volume/mass ratios are comparable, with 2.27 and 2.18 Å^3/Da corresponding to a solvent content of 0.49 and 0.436 for talin1 and talin2, respectively. The crystal contacts in the talin1 structure (Fig. S2 and Tables 3 and 4) were already analyzed by the University of Leicester team (50) and Campbell (51) and were not thought to contribute to the talin1 conformation. In our talin2 crystal, the screw axis packs the talin2 F1 subdomain against F0' from a symmetry-related molecule (Fig. S3*A*) and allows for F1-F1' (Fig. S3*C*) or F3-F0' (Fig. S3*D*) intramolecular interactions, whereas the crystal is held together along the *y* axis through F0-F2' intramolecular interactions (Fig. S3*B*).

Regions that engage in talin2 intersubdomain-specific interactions involve residues 198–211 that connect F1 and F2 and those that are in proximity of F2 (residues 120–129), whereas the last F2 α-helix (residues 294–309) is also engaging in intradomain F1-F2 contacts (Fig. 1*B*). These unique interactions provide the novel talin2 cloverleaf-like constellation that is distinct not only from the talin1 linear arrangement but also from all other known FERM domain protein structures. For example, whereas kindlin (PDB entry 5XQ1; Fig. S4*A*) also has an additional F0 subdomain (52), the F2-F3 di-domains are oriented distinctly in talin when aligning their respective F0 and F1 subdomains (Fig. S4, *A–C*). For comparison, the constellation of a canonical FERM architecture as, for example, seen in merlin (PDB entry 6CDS) (53) has a kindlin-like architecture (Fig. S4*D*), which again is distinct from that seen in talin.

Interestingly, the pivot point that drives the conversion of the talin1 linear arrangement *versus* the semi-cloverleaf type arrangement in talin2 stems from the positioning of crucial talin2 residues (*e.g.* Lys-198 and Phe-199). In talin2, these residues assume a *cis* conformation leading to stabilized hydrophobic stacking interactions, formed by Ile-132, Trp-175, and Tyr-201, on either side of the already stacked Lys-198 and Phe-199 residues (Fig. 1*B*). However, in talin1, the corresponding Lys-196 and Phe-197 (the numbering differs) are arranged in a *trans* configuration leading to the linear arrangement of the loop preceding the terminal β-strand of the F1 domain (Fig. 1*C*), an interaction that is probably responsible in maintaining the distinct F0-F1 orientation with respect to F2-F3.

Further isoform-specific interactions might result from the long F1 loop (residues 139–170) that is missing in the talin1 structure due to deletion to aid crystallization (50). The F1 loop (residues 144–167) was thought to form an α-helix (54), and this loop is visible for the first time in talin2 (with electron density only missing for residues 143–153) where residues 156–166 form an α-helix (Figs. 1*A* and 2).

Superposition of the F0-F1 domains of the two isoforms reveals that the talin2 F1 loop resides in the space occupied by F2 in the talin1 structure (Fig. S1*C*). The same steric hindrance is seen when superimposing the talin1 F1 solution structure (PDB entry 2KC2) (54) onto the talin1 head structures that have the 139–168 deletion (PDB entries 6MFS and 3IVF) (50, 55) (Fig. S1*D*). Thus, the unknown native full-length talin1 head domain structure must either have its F1 loop distinct from the F1 solution structure, or the talin1 F1-F2 interdomain interactions are distinct from the linear arrangement found in the Δ139-168 talin1 head domain structure.

The inactive mammalian talin isoforms are monomeric

Turkey gizzard talin1 was reported to be a dimer (20). To determine the oligomeric state of mammalian talin, we analyzed full-length talin by multiangle light scattering coupled with size-exclusion chromatography, which also confirmed that our proteins are not misfolded aggregates. We found that both full-length murine talin1 and human talin2 are monomeric in solution (Fig. 3*A*) even though full-length talin2 showed some aggregates. Full-length talin1 exhibited a molar mass of 245.2 g/mol ± 0.6%, which is close to the monomeric estimated mass of 270 kDa with a hydrodynamic radius of 6.8 nm ± 0.2%. Talin2 exhibited a molar mass of 280.4 g/mol ± 1.9% g/mol, which corresponds to the calculated mass of 274 kDa with a hydrodynamic radius of 8.7 nm ± 0.6%, suggesting an overall extended conformation. Likewise, the individual talin

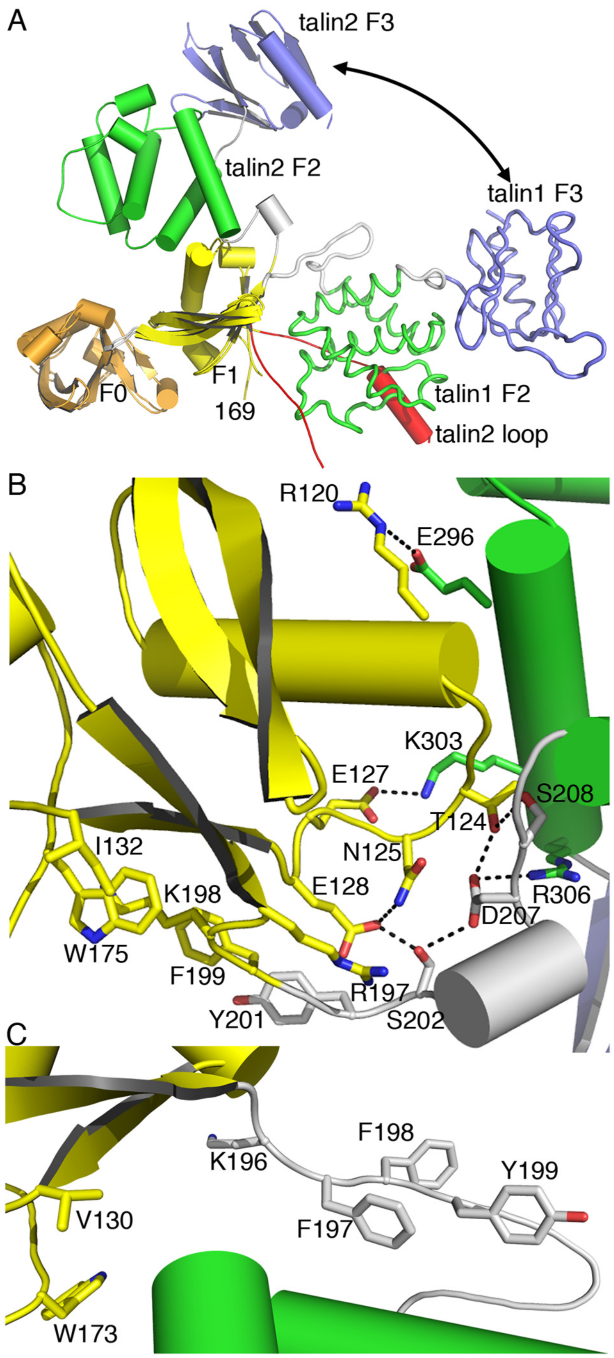

Figure 1. The talin isoforms have distinct FERM domain constellations. *A*, superposition of the F0-F1 di-domains of murine talin1 onto human talin2 (F0, residues 4–83, *orange*; F1, residues 87–199, *yellow*). The talin1 F2 and F3 domains are shown as a *ribbon*, and the talin2 F2-F3 (F2, residues 211–308, *green*; F3, residues 314–402, *blue*) are shown as a *cartoon*. Murine talin1 has its F0-F1 di-subdomain unit aligned linearly with respect to its F2-F3 di-subdomain motif. The F1 loop that is truncated in the talin1 structures (PDB entries 6MFS and 3IVF) (51, 56) is indicated as residue 169. Notably, the talin2 F0-F1 di-subdomains are making talin2-specific interactions with F2-F3. Most of the F1 loop is visible in our talin2 structure (shown in *red*) and harbors an α-helix. Whereas the F2-F3 di-subdomains are rotated ~140° relative to their position seen in talin1 (*double arrow*), the F0-F1 di-subdomains align with root mean square deviation of 0.841 Å for 1,256 atoms. *B*, talin2-specific F1 (*yellow*) interdomain interactions with F2 (*green*). Thr-124 and Glu-128 along with Gly-122 interact extensively with the residues from the F1-F2 linker region. Thr-124 OG1 exhibits interactions with Ser-208 OG (*dotted line*) and N as well as Asp-207 OD2. Glu-128 OE1 and OE2 interact with Arg-197 NH_2 and Ser-202 OG, respectively. Glu-128 OE1 interacts with the backbone Tyr-201 and Ser-202 nitrogens. Gly-122 O is within hydrogen-bonding distance of Ser-208 OG and aids in maintaining the F1-F2 region in proximity to the F1 domain. Thr-124 O along with Glu-127 OE2 contribute toward anchoring the bottom of the last α-helix of F2 domain through Lys-303 NZ interaction. The top of the helix is held in place through Arg-120 NE and Glu-296 OE2 hydrogen-bonding, with the bulk of the stabilization provided by the hydrophobic interactions contributed by Val-299, which is surrounded by Gly-122, Thr-124, and Tyr-126 at a distance of about 4.3 Å. Arg-306 contributes to the stability of this constellation through hydrogen bonding interaction with Val-206 O and Asp-207 OD2. *C*, Distinct talin interdomain interactions. The interface of talin1 F1 (*yellow*) and F2 (*green*) lacks the stable interaction seen in talin2 (*B*) due to the distinct orientation of the Trp-173 side chain and the *trans* conformation of Lys-196 and Phe-197, leading to the linear extension of the F1-F2 linker region (*gray*) and overall linear configuration of the talin1 head domain.

Table 3

Analyses of the crystal contacts of the two talin isoforms by the PDBePISA server (RRID:SCR_015749)

The last column in the table refers to the view of said crystal contact in the indicated figure (Fig. S2 (for *A*) or Fig. S3 (for *B*).

A. The murine talin1 head domain structure, PDB entry 3IVF, residues 1–400 Δ139–168, has a surface area of 20,705 Å^2											
$xyz\ {}^iN_{at}$	$xyz\ {}^iN_{res}$	Symmetry operator	Sym ${}^iN_{at}$	Sym ${}^iN_{res}$	Interface area (Å^2)	Δ^iG (kcal/mol)	Δ^iG p value	N_{hb}	N_{sb}	N_{ds}	Figure
72	23	$x, -y, -z+1$	72	23	726.1	−2.9	0.429	8	6	0	S2*A*
62	17	$-x-1, y-1/2, -z+1/2$	59	22	562.5	2.2	0.737	8	2	0	S2*B*
53	18	$-x-1, -y+1/2, z-1/2$	60	15	540.0	−0.2	0.535	9	5	0	S2*C*
47	13	$x-1, y, z$	48	14	386.8	−1.3	0.415	3	0	0	S2*D*
2	1	$-x, y-1/2, -z+1/2$	5	2	51.9	1.7	0.909	0	0	0	S2*F*
2	2	$x, -y+1, -z+1$	2	2	16.4	0.8	0.878	0	0	0	S2*E*
B. Our human talin2 head domain structure, residues 1–403, has a surface area of 23,822 Å^2											
129	39	$x-y, x-1, z-1/6$	145	39	1,165.2	−14.6	0.160	6	0	0	S3*A*
83	27	$x, y-1, z$	83	26	775.3	−4.9	0.433	3	4	0	S3*B*
60	22	$x-y, x, z-1/6$	68	25	547.2	−0.8	0.652	2	0	0	S3*C*
37	11	$x-y+1, x-1, z-1/6$	33	10	334.6	−4.4	0.258	1	0	0	S3*D*
17	6	$x-y+1, x, z-1/6$	21	6	171.1	−0.9	0.531	2	1	0	
19	6	$-y, x-y-1, z-1/3$	11	2	137.3	0.1	0.650	2	0	0	
10	3	$-y+2, x-y, z-1/3$	15	5	126.8	−1.4	0.386	0	0	0	
10	6	$x-1, y-1, z$	11	4	86.0	0.1	0.576	0	0	0	
1	1	$x-y-1, x-1, z-1/6$	1	1	2.7	0.1	0.763	0	0	0	

head domains were predominantly monomeric (Fig. 3*B*) and exhibited molar masses of 42.4 g/mol ± 0.6% and 44.9 g/mol ± 0.7% for the talin1 (residues 1–400) and talin2 (residues 1–403), respectively. Interestingly, despite the differences in the talin1 and talin2 respective subdomain arrangements, the hydrodynamic radii were similar, 3.3 nm ± 0.3% and 3.2 nm ± 0.4%, respectively. While our manuscript was under review, the full-length human talin1 structure was also shown to be monomeric (49).

The inactive mammalian talin isoforms bind lipid vesicles

To confirm that our recombinant talin proteins are functional, we tested their binding to the membrane. The talin rod domain was thought to hinder binding of full-length inactive talin to the membrane (56). Superposition of the F3 subdomain of our talin2 structure onto the F3 subdomain of the talin1 head/tail complex structure (PDB entry 4F7G) (57) (Fig. 4*A*) shows that talin1 Gly-376 is replaced by talin2 Ser-379 and too close to Asp-1676 from the talin1 rod domain. Talin1 Asp-1676 corresponds to talin2 Glu-1678, and the larger side chains on both head and tail domains (Ser/Glu *versus* Gly/Asp) make this talin1 interaction thus unlikely in talin2. Further, talin1 Met-1802 corresponds to talin2 Leu-1804, which again is too close to conserved Gly-321 (corresponding to Gly-324 in talin2). It remains to be seen whether the full-length talin2 structure has the same head-tail interface as seen in talin1.

Because most membrane-binding experiments were performed with individual talin domains (*e.g.* the F3 FERM subdomain and residues 1,654–2,344, termed talin-R$_M$ for talin rod middle segment, from the talin1 rod domain) (50, 56, 58, 59), we performed lipid co-sedimentation assays with full-length proteins. In agreement with the earlier experiments from individual domains (58), our full-length talin1 did not bind phosphatidylcholine (PC). However, we found that full-length talin1 bound PIP$_2$ (Fig. 4*B*). Because the F3 interaction with talin-R$_M$ is disrupted by PIP$_2$ (56), our data suggest that PIP$_2$ binding to talin is the first step in integrin inside-out activation. Further, the N-terminally truncated talin1 constructs with (residues 437–2,541) and without (residues 437–2,493) the "dimerization domain" did not bind PIP$_2$ or PC (Fig. 4*C*). Thus, our recombinant proteins are functional with respect to membrane localization, and full-length inactive talin binds the plasma membrane. The PIP$_2$-binding site resides on the talin head domains.

The talin R9 domain (residues 1,655–1,822) is part of the above mentioned talin-R$_M$ domain (residues 1,654–2,344) and in talin1 was initially implicated in autoinhibitory regulation through its interaction with the F3 subdomain (residues 311–398) (60). The recently determined talin1 cryo-EM structure showed that in addition to the head-tail F3-R9 interaction, another head-tail interaction between F2 (residues 209–304) and R12 (residues 2,131–2,291) further prevents integrin and phospholipid binding to talin and confirmed that the lipid- and tail-binding sites are overlapping on the talin head domain and the integrin-binding site is obstructed by the tail domain (49). Collectively, our data provide mechanistic insights into how talin binding to the cell membrane relieves the talin autoinhibition.

The talin isoforms share the same lipid-binding site

We identified the *bona fide* talin1 lipid-binding site (that is strictly conserved in the two mammalian talin isoforms, residues K272Q, K316Q, K324Q, E342Q, and K343Q) structurally, biochemically, and functionally (Fig. 5). The talin1 PIP$_2$-bound and -unbound structures are very similar (Fig. 5*B*) (55). However, when superimposing the F2 subdomains of our PIP$_2$-bound talin1 and apo-talin2 structures, residue Lys-324 of the talin1 lipid-binding loop is moved by about 7 Å in the unbound talin2 structure (Fig. 5*C*). Despite significant attempts, we were unable to capture the talin2/PIP$_2$ complex crystal structure. Thus, we mutated the equivalent talin2 residues that were identified as *bona fide* lipid binders in talin1 and cross-verified the structural integrity through thermal shift analyses, which exhibited a melting temperature (T_m) comparable with the WT, representing a well-folded protein (Fig. 5*D*). We performed lipid co-sedimentation assays and found that the talin2 equivalent mutant (K274Q, K319Q, K327Q, E345Q, and K346Q) did not bind to vesicles at all (Fig. 5*E*). Thus, the

Table 4

Residues involved in crystal contacts in the two talin isoform structures as identified by the PDBePISA server (RRID:SCR_015749)

A. Crystal contacts in the talin1 head domain structure (residues 1–400 Δ139–168)

i. Fig. S2A	**Distance (Å)**	**$x, -y, -z + 1$**
Tyr-70 OH	2.70	Asp-208 OD2
Arg-74 NH1	2.75	Asp-222 OD2
Arg-74 NH$_2$	3.30	Asp-222 OD1
Gln-211 NE2	2.90	Tyr-70 O
Asp-208 OD2	2.70	Tyr-70 OH
Asp-222 OD2	2.75	Arg-74 NH1
Asp-222 OD1	3.30	Arg-74 NH$_2$
Tyr-70 O	2.90	Gln-211 NE2
Arg-74 NH1	2.75	Asp-222 OD2
Arg-74 NH$_2$	3.30	Asp-222 OD1
Arg-74 NH$_2$	3.35	Asp-222 OD2
Asp-222 OD2	2.75	Arg-74 NH1
Asp-222 OD1	3.30	Arg-74 NH$_2$
Asp-222 OD2	3.35	Arg-74 NH$_2$
Arg-358 NE	2.92	Lys-284 O

ii. Fig. S2B	**Distance (Å)**	**$-x - 1, y - 1/2, -z + 1/2$**
Arg-358 NH$_2$	2.99	Asn-285 O
Trp-359 N	3.01	Asn-285 OD1
Tyr-377 N	2.80	Asp-94 O
Lys-357 O	3.35	Gln-281 NE2
Ala-361 O	2.75	Arg-297 NH1
Gln-390 OE1	3.47	Lys-234 NZ
Asp-397 OD2	2.87	Lys-278 NZ
Asp-397 OD1	3.92	Lys-278 NZ
Asp-397 OD2	2.87	Lys-278 NZ

iii. Fig. S2C	**Distance (Å)**	**$-x - 1, -y + 1/2, z - 1/2$**
Lys-322 NZ	3.60	Arg-33 O
Arg-328 NH1	3.22	Arg-35 O
Arg-339 NH1	3.00	Glu-38 OE1
Arg-339 NH$_2$	2.79	Glu-38 OE2
Lys-320 NZ	3.44	Ala-41 O
Ile-348 O	2.86	Val-14 N
Asp-341 OD1	2.91	Lys-15 NZ
Glu-346 OE1	2.80	Thr-16 N
Glu-346 OE2	2.75	Thr-16 OG1
Arg-339 NH1	3.00	Glu-38 OE1
Arg-339 NH$_2$	3.68	Glu-38 OE1
Arg-339 NH1	3.36	Glu-38 OE2
Arg-339 NH$_2$	2.79	Glu-38 OE2
Asp-341 OD1	2.91	Lys-15 NZ

iv. Fig. S2D	**Distance (Å)**	**$x - 1, y, z$**
Asn-123 ND2	3.35	Glu-252 O
Arg-207 NH1	2.91	Gly-258 O
Arg-207 NH1	2.71	Leu-260 O

B. Crystal contact in our talin2 head domain structure, residues 1–403

i. Fig. S3A	**Distance (Å)**	**$x, -y, -z + 1$**
Arg-11 NH1	3.73	Arg-306 O
Arg-11 NH1	3.90	Leu-308 O
Ser-54 N	3.16	Tyr-201 OH
Ser-54 OG	3.20	Phe-200 N
Ile-80 O	2.75	Tyr-201 OH
Phe-249 O	3.89	Tyr-376 OH

ii. Fig. S3B	**Distance (Å)**	**$-x - 1, y - 1/2, -z + 1/2$**
Arg-59 NH1	3.27	Leu-262 O
Glu-137 OE2	3.18	Lys-265 NZ
Asp-55 OD2	3.87	Arg-276 NH1
Arg-59 NH1	3.12	Glu-279 OE1
Arg-59 NH1	3.00	Glu-279 OE2
Glu-137 OE2	3.18	Lys-265 NZ
Asp-55 OD2	3.87	Arg-276 NH1

iii. Fig. S3C	**Distance (Å)**	**$-x - 1, -y + 1/2, z - 1/2$**
Arg-281 NH$_2$	3.30	Lys-166 O
Arg-281 NH$_2$	3.87	His-168 O

iv. Fig. S3D	**Distance (Å)**	**$x - 1, y, z$**
Thr-69 OG1	3.46	Asn-326 O

Table 4—*Continued*

v. Fig. S3F	**Distance (Å)**	**$-x, y - 1/2, -z + 1/2$**
Arg-276 NH$_2$	3.74	Pro-366 O
Lys-346 NZ	3.24	Glu-389 OE2
Lys-346 NZ	3.24	Glu-389 OE2

vi. Fig. S3E	**Distance (Å)**	**$x, -y + 1, -z + 1$**
Val-38 O	2.93	Arg-155 NH$_2$
Arg-35 O	2.54	Arg-155 NH$_2$

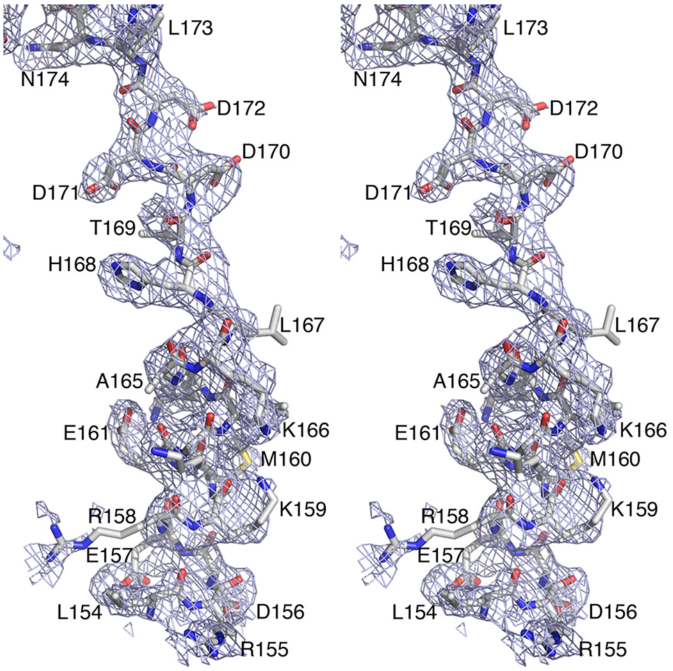

Figure 2. Final $2F_o - F_c$ electron density map at 2.56 Å resolution contoured at 2.5σ of our human talin2 structure, residues 1–403. Shown is a crosseye stereo view of the F1 loop that was truncated in the talin1 structure.

talin2 head domain has a single membrane attachment site that is conserved in talin1.

To measure the association of the talin isoforms with the cell membrane in living cells, we developed a FRET-based sensor between the monomeric enhanced GFP (mEGFP)-tagged talin isoforms and a plasma membrane–targeted mCherry (mCherry-CAAX). WT and lipid binding–deficient mutant talin proteins were expressed in papillary collecting duct cells in a *talin*$^{-/-}$ knockout background, together with the membrane-targeted mCherry fluorophore (Fig. 6*A*). When talin-GFP– and the CAAX–mediated membrane-localized mCherry are in proximity (<10 nm), FRET between them occurs and was measured through FLIM-FRET (61). Calculation of the fraction of overexpressed talin bound to the membrane (binding fraction) was quantified based on lifetime measurements and compared with (i) control cells expressing only GFP, (ii) GFP- and membrane-targeted mCherry with and without the unlabeled talin isoforms, and (iii) GFP-tagged talin isoforms without mCherry (Fig. S5*A*). Importantly, expressing either unlabeled or GFP-tagged talin proteins in the *talin*$^{-/-}$ knockout background induced a similar robust spreading morphology as well as formation of focal adhesion and stress fiber formation.

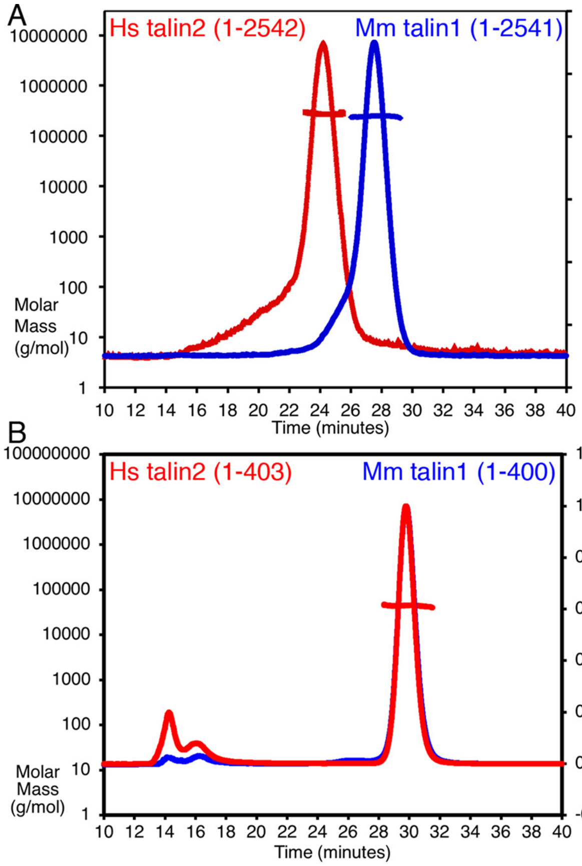

Figure 3. MALS coupled with SEC to determine the absolute mass of talin. The *right ordinate* represents the light scattering (*V*). *A*, full-length murine talin1 (residues 1–2,541, *blue trace*) and full-length human talin2 (residues 1–2,542, *red trace*) show similar monomeric molar masses of 245.2 and 280.4 kDa, respectively, as calculated by the Astra software with notable differences in the conformation as represented by their varied hydrodynamic radius for the two proteins. The apparent masses as calculated from the polypeptide chains are 270 and 274 kDa, respectively. *B*, the murine talin1 (residues 1–400) and human talin2 (residues 1–403) head domains exhibited similar hydrodynamic radii and monomeric molar masses of 42.4 and 44.9 kDa, respectively. The apparent masses as calculated from the polypeptide chains are 46.6 and 47 kDa, respectively.

Thus, the GFP-tagged talin isoforms were functional and localized as seen for WT talin. Immunoblotting showed robust expression of WT and mutant proteins, suggesting that the impaired cell spreading in cells expressing the lipid binding–deficient mutants is indeed due to defective lipid binding (Fig. 6*B*).

Both talin isoforms showed significant binding to the cell membrane ($p < 0.0001$; Sidak's multiple-comparison test after one-way ANOVA), and mutations in talin1 and talin2 that disrupt PIP$_2$ binding *in vitro* significantly impaired this association in live cells. In addition, our data suggested that talin2 binds the membrane more robustly than talin1 (Fig. 6*C*), which was supported by PIP$_2$ vesicle pulldowns that showed a higher maximum binding for talin2 compared with talin1 (55% *versus* 37%, respectively) (Fig. 6*D*). Their binding constants were similar (3.4 and 4.6 μM for talin2 and talin1, respectively) and also comparable with binding affinities determined for a different FERM domain protein (focal adhesion kinase; 6 μM) (62). These findings were significant irrespective of relative expression levels of the talin constructs or the relative ratio of GFP-talin relative to membrane-localized mCherry (Fig. S5).

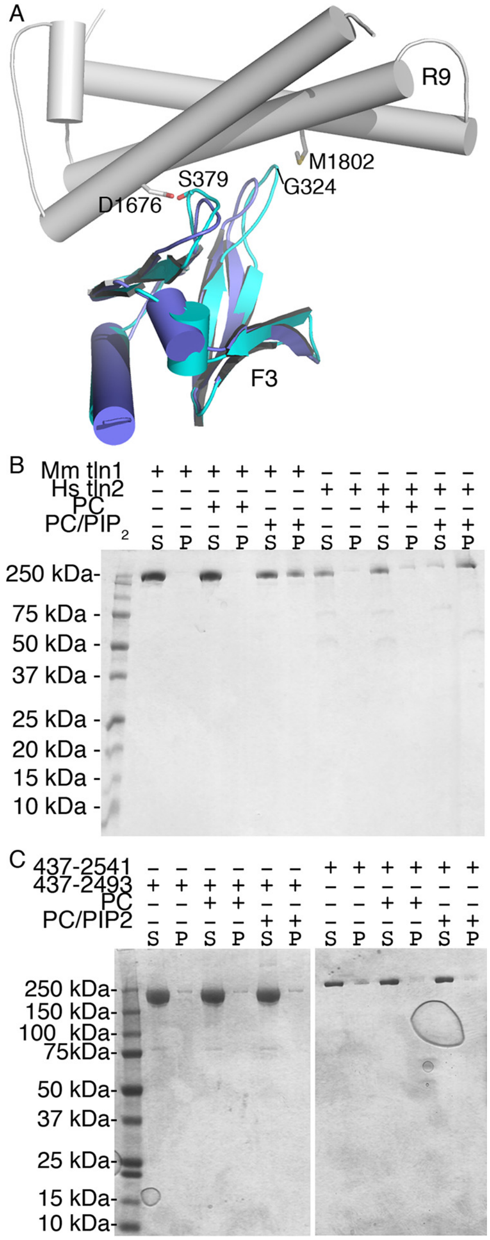

Figure 4. The F3 autoinhibited interface harboring the lipid binding site is distinct in the two talin isoforms. *A*, superposition of the F3 subdomains (residues 314–402) of our talin2 structure (*cyan*) onto talin1 (*blue*) in complex with the R9 talin1 rod domain (residues 1,655–1,824; *gray*; PDB entry 4F7G) (58) with root mean square deviation of 0.525 Å (for 544 atoms). Notably, talin1 Gly-376 is replaced by talin2 Ser-379 and too close to Ala-1676 from the talin1 rod domain. Talin1 Ala-1676 corresponds to talin2 Glu-1678, and the larger side chains on both head and tail domains (Ser/Glu *versus* Gly/Asp) make this talin1 interaction thus unlikely in talin2. Talin1 Met-1802 corresponds to talin2 Leu-1804, which again is too close to conserved Gly-321 (corresponding to Gly-324 in talin2). *B*, lipid co-sedimentation assays of full-length murine (*Mm*) talin1 (residues 1–2,541) and human (*Hs*) talin2 (residues 1–2,542). *S*, supernatant; *P*, pellet. *C*, lipid co-sedimentation assays of the talin1 rod domain with (residues 437–2,541) and without (residues 437–2,493) the "dimerization domain." *S*, supernatant; *P*, pellet. Compared with full-length talin proteins (*B*), there is some aggregation seen with the N-terminally truncated talin proteins in the absence of lipids.

Confocal microscopy studies support the observation that overexpression of WT talin in papillary collecting duct cells on

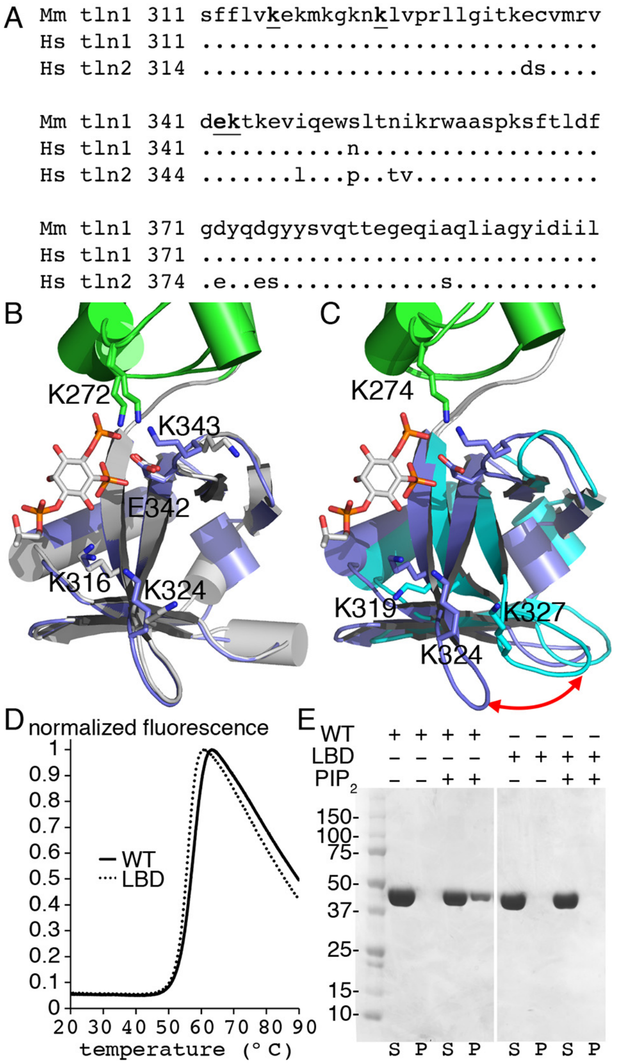

Figure 5. Talin attachment to the plasma membrane. *A*, F3 sequence alignment of talin1 from *Mus musculus* (*Mm*) and *Homo sapiens* (*Hs*) talin1 and talin2. Talin1 residues Lys-316, Lys-324, Glu-342, and Lys-343 are *underlined* to emphasize their role in lipid binding. *B*, superposition the F2 subdomains (*green*, talin1 residues 209–304) of the lipid-bound talin1 structure (F3 in *blue*) (PDB entry 6MFS) (56) onto the unbound talin1 structure (F3 in *gray*) (PDB entry 3IVF) (51) suggests that the unbound talin1 structure is in its activated state. *C*, superposition of the F2 subdomains (*green*, talin2 residues 211–308) of our talin2 structure onto the lipid-bound talin1 structure (PDB entry 6MFS) (56) shows the relative orientation of F3 (talin1, *blue*, residues 311–400; talin2, *cyan*, residues 314–403). Talin1 residue Lys-324 that binds PIP_2 is moved by about 7 Å in the unbound talin2 structure indicated by a *red double arrow*. Lipid-binding residues are *labeled* in both isoforms. *D*, normalized thermal denaturation profiles of WT (*solid line*) and lipid binding–deficient (LBD) mutant (K274Q, K319Q, K327Q, E345Q, and K346Q; *dashed line*) talin2 indicates that both talin isoforms have similar transition temperatures (57.02 ± 0.11 and 55.52 ± 0.03 °C, respectively). Averages of triplicate measurements as obtained with SYPRO orange dye were plotted for the determination of the melting temperature, T_m. *E*, lipid co-sedimentation assays of human WT and LBD mutant (K274Q, K319Q, K327Q, E345Q, and K346Q) talin2. *S*, supernatant; *P*, pellet.

a *talin*$^{-/-}$ knockout background showed robust spreading, focal adhesions, and actin stress fiber formations (Fig. 7). We used band pass filtering and threshold application to calculate the total cell areas and the focal adhesion areas (Fig. 8). The morphology of cells was clearly reflected in the total cell area analyses (Fig. 8*A*). Cells expressing the lipid binding–deficient talin mutants had a mean total area of ~250 μm^2, whereas those expressing WT talin showed a much larger cell spread (~500 μm^2 for talin1 and ~350 μm^2 for talin2) (Fig. 8*B*). The effect of expressing the lipid binding–deficient mutant on the cell spread was also demonstrated by Sidak's multiple-comparison tests, within ordinary one-way ANOVA, with an adjusted p value of <0.0001. Whereas the focal adhesion sizes in the cells expressing WT or mutant proteins were similar (Fig. 8*C*), the focal adhesion area was on average about 0.17 μm^2 for talin1 and about 0.13 μm^2 for talin2. The value observed for the WT is comparable with the size reported previously for such focal adhesions in papillary collecting duct *talin* knockout cells (33). Sidak's comparison test did not reveal any significant difference between cells expressing WT and mutant proteins. However, the focal adhesion size appeared to be larger for talin1 compared with talin2 (Fig. 8*C*). Collectively, binding of talin2 to the cell membrane is crucial for talin2 in regulating various cell functions, including migration, adhesion, and maintenance of cellular integrity.

Discussion

Isoform-specific talin head domain structures and functions

Talin is the key cytoplasmic protein that mediates integrin adhesion to the extracellular matrix (63) and acts as a bridge between the cytoskeleton and the extracellular matrix. Talin is of great interest to the field of mechano-biology as it unfolds and exposes cryptic vinculin-binding sites under force stimulation. Significantly, when talin activators are dysregulated, abnormal integrin activation and mechano-transduction lead to changes in cell migration and spreading and cell survival that result in various diseases (64).

Talin has two main functional units, the N-terminal head (residues 1–400) and the C-terminal tail (residues 437–2,541), that are connected by a calpain-susceptible linker region. The two most important functions of the head domain are its binding to and activation of integrin and its binding to the plasma membrane (4, 5). These interactions are regulated by the head domain binding to the autoinhibition site on the talin tail domain. Our structural and biochemical data support a mechanism whereby the plasma membrane severs the talin autoinhibitory head-tail interactions.

Vertebrae have two talin isoforms with ~76% sequence identity (~88% sequence similarity) throughout the polypeptide chain. Talin1 was discovered 35 years ago (65) in chicken gizzard smooth muscle and was found to target to focal adhesions and membrane ruffles. Talin2 was discovered more recently via the sequencing of the human genome. Whereas *talin1* knockout is embryonic lethal (42), *talin2* knockout mice are viable and fertile, although they display a mild dystrophic phenotype (66).

Talin1 has been extensively studied, and all individual domain structures have been determined by X-ray crystallography or NMR (25, 26, 28, 34, 50, 54, 67–71), negative stain microscopy (20), and more recently by cryo-EM (49). However, with the exception of the talin2 F2-F3 domains bound to integrin β1D (67), there is no structural information available on any other talin2 domain. The talin1 FERM domain structure determination challenged the view that FERM domains are uniform superfolds

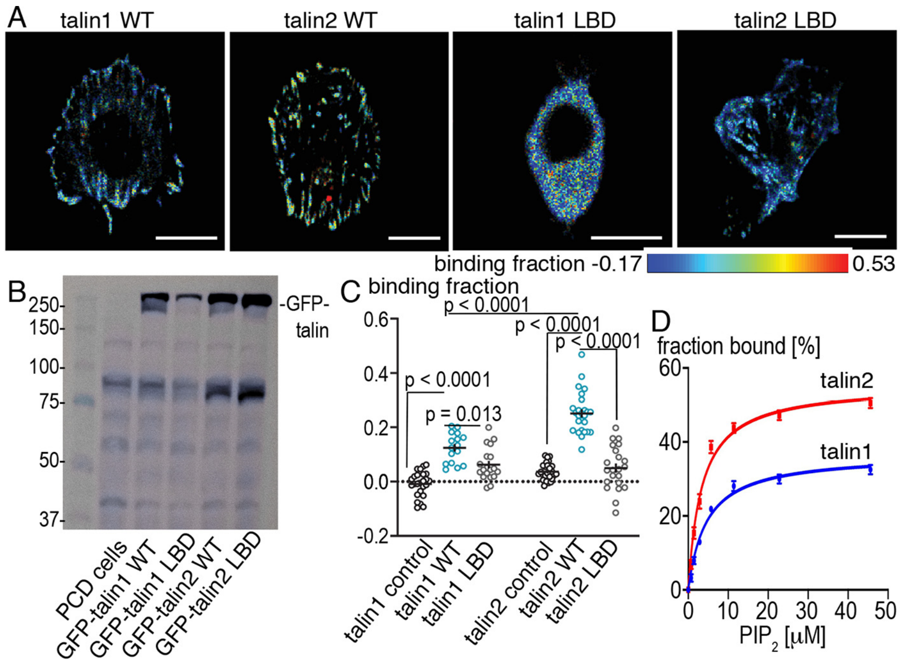

Figure 6. Talin attachment to the plasma membrane in cells depends on its binding to PIP$_2$. *A*, fluorescence lifetime images of WT or LBD mutant talin expressed in papillary collecting duct cells on a *talin*$^{-/-}$ background. The FRET-based sensor consisted of two components, mEGFP-tagged talin isoform and a plasma membrane–targeted mCherry by a K-Ras–derived CAAX domain. *Scale bar*, 10 μm. The spectrum represents the range of binding fraction from -0.17 (*blue*) to 0.53 (*red*). *B*, the expression of the full-length talin proteins used for FLIM experiments was confirmed with the anti-GFP antibody. *C*, quantification of the binding fractions between talin proteins and the mCherry-labeled membrane using FLIM. Control experiments consisted of mEGFP-tagged talin isoforms expressed in the absence of the membrane-targeted mCherry acceptor. *Circles*, individual cells; *lines*, mean ± S.E. ($n = 16$–25 cells). Statistics indicated are *p* values from Sidak's multiple-comparison tests between the indicated groups after one-way ANOVA ($F(3, 68) = 59.38.07$, $p < 0.0001$). *D*, vesicle pulldown assays with 6% (mol/mol) PIP$_2$ vesicles and talin1 (residues 1–400; *blue*) or talin2 (residues 1–403; *red*). Talin2 showed higher maximum binding compared with talin1 (55.5% *versus* 36.8%, respectively). Both isoforms have similar binding affinities with dissociation constants (K_d) of 4.6 ± 0.5 μM for talin1 and 3.4 ± 0.3 μM for talin2. *Error bars*, S.D. from three independent experiments. K_d values were determined by fitting a one-site binding model. The obtained fitting r^2 values were 0.9848 for talin1 and 0.9851 for talin2.

that are stabilized in a globular cloverleaf arrangement as its F1 domain aligns linearly with the F2-F3 di-domains.

We determined the crystal structure of the entire talin2 head domain without an engineered truncation that deletes residues 139-168 in the structure of the talin1 head domain (50, 55). The full-length talin1 F1 subdomain structure (54) suggested that these residues could be deleted without affecting the structure of F1. Superposition of our full-length talin2 head domain structure onto the truncated talin1 head domain structure (50) shows that in talin2, residues 139–168 are occupying the corresponding space where F2 interacts with F1 in talin1. This steric hindrance is also evident when superimposing the talin1 F1 solution structure (PDB entry 2KC2) (54) onto the truncated talin1 head domain structures (PDB entries 6MFS and 3IVF) (50, 55) where the talin1 F1 loop prevents the F1-F2 interaction seen in the truncated talin1 head domain structure. Although residues 171–174 at the C terminus of the F1 loop in talin1 fold back toward F0-F1 but away from F0-F1 in talin2, these loops protrude similarly from the ubiquitin-like F1 domain into the space currently occupied by F2 in the talin1 structure. It remains to be seen how the F1 loop is positioned in the talin1 head domain.

Because the double subdomain units of F0-F1 or F2-F3 are similar in both talin isoforms, and the latter is as seen in all other FERM domain structures, the subdomain interactions between the F1 and F2 subdomains are unique and isoform-specific. Indeed, no other FERM domain has been determined that had the arrangement seen in our talin2 structure. Our talin2 structure shows that the F2-F3 di-domains and the F0-F1 di-domains seem to be the structural building blocks of FERM domains that can arrange in distinct ways by varying the F0-F1 interaction with F2-F3 while the interfaces between F0 and F1 or F2 and F3 are conserved. It is intriguing how proteins use the same F0-F1 and F2-F3 di-subdomain building blocks and arrange these differently in the tertiary structure.

The talin1 head domain showed an angle of ~125° between the F0-F1 and F2-F3 di-domains as determined by SAXS (50) compared with 155° angle observed in the linear arrangement of the crystal structures (PDB entries 6MFS and 3IVF) (50, 55). Such flexibility between F1 and F2 was also noted by SAXS data from the human talin1 head domain (50). Indeed, in the full-length talin1 cryo-EM structure, F0-F1 were not visible, again suggesting flexibility between the F0-F1 and F2-F3 di-domains. Whereas the effects of crystal contacts cannot be completely ruled out in a potential or no role of a certain F0-F1 orientation relative to the F2-F3 double subdomains, the collective structural and biochemical data suggest that the isoform-specific amino acid sequence dictates its configuration. It is thus likely that we will uncover many other variations of this tertiary arrangement.

The talin isoforms are monomers

Originally, talin1 was isolated from chicken gizzard and was reported to be in an equilibrium between a monomer and a

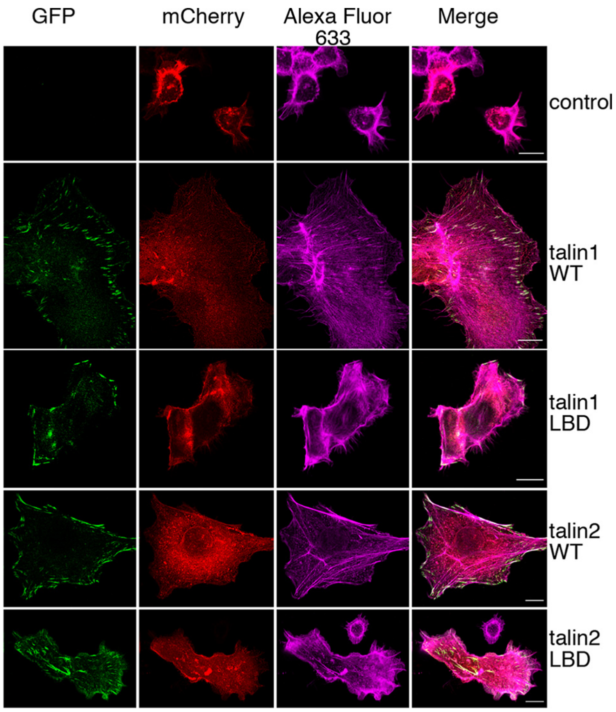

Figure 7. PIP$_2$ confers membrane-mediated activation of talin. Papillary collecting duct cells with a *talin*$^{-/-}$ background, transiently co-expressing full-length WT or LBD mutant (K274Q, K319Q, K327Q, E345Q, and K346Q) murine GFP-talin1 or human GFP-talin2 with mCherry-CAAX, were fixed and immunostained for F-actin with Alexa Fluor 633 phalloidin. High-resolution confocal images were obtained to show the expression of GFP-talin (*green*), mcherry-CAAX (*red*), and F-actin (*magenta*). Significant differences were observed due to the overexpression of WT and mutant talin, highlighting the requirement of the talin-PIP$_2$ association for talin attachment to the cell membrane. *Scale bar*, 10 μm.

dimer (72). We overcame the tendency of talin to aggregate and eliminated contributions from impurities of proteins that are enriched when isolating talin from gizzards by using highly purified recombinant proteins. We determined the absolute mass of mammalian full-length talin1 and talin2. Our multiangle light-scattering experiments clearly show that murine talin1 and human talin2 are monomeric as had also been determined for human talin1 (49) while our manuscript was in review. Similarly, the isolated head domains (residues 1–400 for talin1 and 1–403 for talin2) were monomeric. The different elution times of the full-length proteins further suggest that the full-length proteins have an isoform-specific tertiary structure. Thus, the functional differences of the talin isoforms are evident on a primary, secondary, and tertiary structural level.

In the crystal structure, the talin1 F0 subdomain engages in extensive 2-fold related contacts with a symmetry-related F2′ that creates an antiparallel dimer. Residues in this F0-F2′ interface are conserved between the two isoforms, so these could occur in talin2, but given that talin2 is not linear, it would explain the aggregation observed in our size-exclusion chromatography (SEC)-multiangle light scattering (MALS) as F0 from one talin2 polypeptide chain could engage in interactions with F2′ from a second talin2 polypeptide chain, whereas its F2 subdomain could simultaneously interact with F0′′ from a third talin2 polypeptide chain. In the talin2 crystal, the F1 loop of one talin2 molecule stretches over F2′ from a second talin2 molecule to interact with F0′′ of a third talin2 molecule. Talin2 crystal contacts also involve an extensive interface comprising F0 with all three FERM subdomains (F1′, F2′, and F3′) of a symmetry-related molecule.

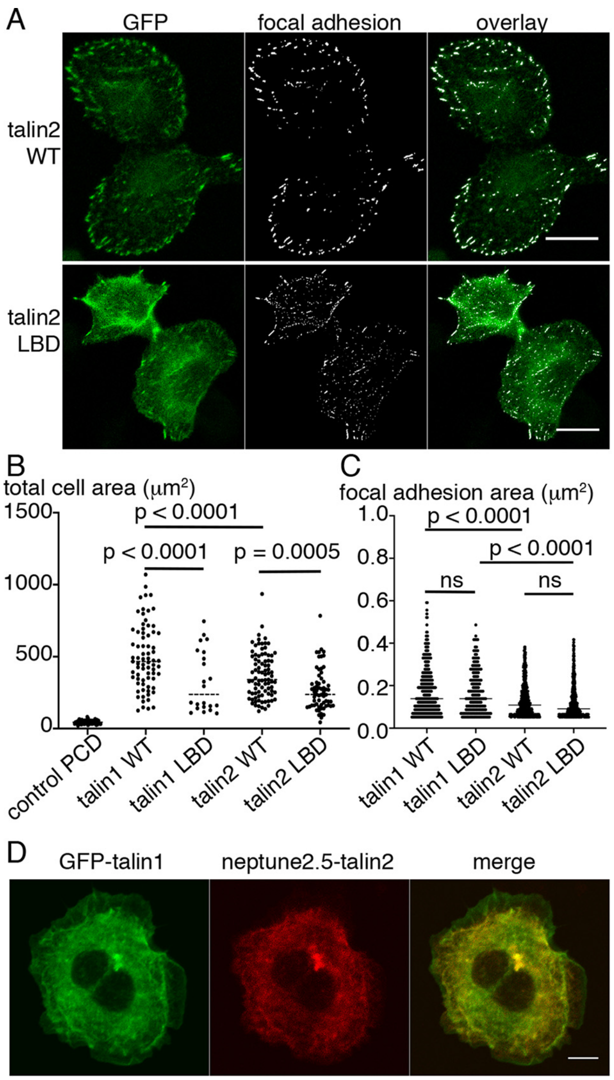

Figure 8. Membrane attachment of talin is necessary for cell adhesion. *A*, the focal adhesion area, seen as *green specks* on the GFP channel is extracted through band pass filtering, threshold, and particle analysis in Fiji is as shown. Representative images for the GFP-talin2 WT (*top*) and LBD mutant (*bottom*) are shown with overlay of the outline of focal adhesions over the image of GFP-talin2–expressing cells. *B*, the total cell areas, measured after applying band pass filtering, threshold, and particle analysis, are shown for the nontransfected control papillary collecting duct cells ($n = 61$), WT GFP-talin1 ($n = 73$), mutant GFP-talin1 ($n = 22$), WT GFP-talin2 ($n = 87$), and mutant GFP-talin2 ($n = 63$). The comparison shows mutant constructs exhibiting significant reduction in cell spreading for both isoforms. *C*, the focal adhesion areas for WT GFP-talin1 ($n = 300$), mutant GFP-talin1 ($n = 188$), WT GFP-talin2 ($n = 463$), and mutant GFP-talin2 ($n = 475$) were determined and plotted for comparison. The focal adhesion area analyses show significant differences as observed by Sidak's multiple-comparison test $p < 0.0001$ between the isoforms. However, the mutants seem unaffected by the size of their focal adhesions. The *p* test values derived from one-way ANOVA analyses were provided for the pairs analyzed in *B* and *C*. *D*, co-expression of talin proteins as GFP- and Neptune2.5-tagged constructs shows similar expression of both constructs within the same cells. *Scale bars*, 5 μm.

The talin isoforms share the membrane attachment site

PIP$_2$ is one established talin activator (73) and contributes to integrin activation by talin recruitment to the plasma membrane,

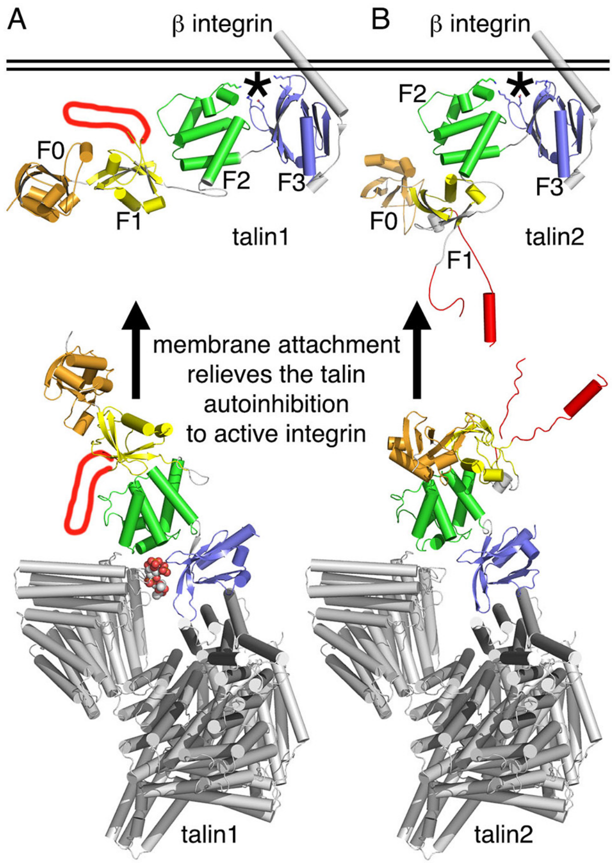

Figure 9. Talin isoform–specific membrane anchoring. Superposition of the unbound F2-F3 subdomains of talin1 (*A*) or talin2 (*B*) onto the integrin β1D-bound talin2 F2-F3 structure (PDB entry 3G9W) (68). For clarity, only integrin (residues 750–788) is shown (in *gray*) of the talin/integrin structure. The talin subdomains are *colored spectrally* (F0 (*orange*), F1 (*yellow*), F2 (*green*), and F3 (*blue*)). The *asterisks* highlight the lipid-binding residues shown in *stick representation*. The talin2 F1 loop, shown in *red* (residues 130–174), is intracellular, even when taking into account that the loop might be very flexible in solution compared with the crystal structure, while in talin1, it is oriented toward the membrane (drawn in *red*). A space-filling model of the PIP$_2$ ligand of our talin1/PIP$_2$ crystal structure is shown to highlight (i) its location within our full-length talin1 model and (ii) the steric hindrance.

where talin then activates integrin (54, 67, 74). The amount of active talin that has its head-tail interaction severed determines adhesion formation. It remains to be seen where the equilibrium between open and closed talin conformer lies.

Whereas charge reversal mutant studies of the isolated F1 loop peptide (residues 139–168, which is ~3% of the entire talin polypeptide chain) alone or of the isolated F1 domain suggested its binding to small unilamellar vesicles and thus suggested that the F1 loop is involved in binding to the plasma membrane (54), such mutagenesis of full-length talin is missing. Notably, superposition of the unbound F2-F3 subdomains of either talin isoform onto the integrin β1D-bound talin2 F2-F3 structure (PDB entry 3G9W) (67) shows that for talin2, the F1 loop is intracellular, whereas in talin1, it is oriented toward the membrane (Fig. 9). This is still the case when taking into consideration that the loop might be very flexible in solution and all sterically possible configurations. Thus, at least for talin2, the F1 loop is not involved in binding to the membrane as previously proposed (54).

Immunostaining studies and mutagenesis strongly support our observation that binding of talin to the membrane is critical to efficiently carry out its cellular functions related to adhesion and maintaining cellular integrity, as evidenced by the lack of actin stress fibers and reduced focal adhesions. Indeed, overexpression of mutant talin proteins in papillary collecting duct *talin* knockout cells showed limited spreading and impaired focal adhesion formation compared with WT cells. Thus, the downstream talin signaling cascade is severely affected. Clearly, membrane attachment of talin is important to tether integrin to the actin cytoskeleton. The periphery of cells expressing the talin PIP$_2$ binding–deficient mutants displayed focal adhesion-like features, and about 50% of talin1 or 20% of talin2 still bound to the cell membrane, perhaps through the ~10-fold weaker interactions of talin with other acidic phospholipids, such as phosphatidylserine (58, 59). Collectively, our structural, biochemical, and functional data provide significant new molecular insights into the talin isoform–specific cell attachment mechanisms that contribute to the various cell adhesion functions.

Experimental procedures

DNA constructs

Talin2 head domain residues 1–403 were cloned using full-length human talin2 as a template into a modified pET-28a vector (EMD Millipore) with an N-terminal octahistidine tag followed by a PreScission protease cleavage site. Mutant talin2 (K274Q, K319Q, E345Q, K346Q, and K327Q) head domain (residues 1–403) was generated by site-directed mutagenesis from the WT talin2 using Agilent Technology's QuikChange site-directed mutagenesis kit.

Full-length human talin2 (residues 1–2,542) and the rod domains of murine talin1 (residues 437–2,541 and 437–2,493) were cloned similarly into modified pET-28a vector to have an N-terminal octahistidine tag with a PreScission protease cleavage site. Full-length murine talin1 was cloned in pET30a vector to have a C-terminal octahistidine tag using standard cloning protocols.

For immunostaining and FLIM studies, full-length talin1 (residues 1–2,541) and its lipid binding–deficient mutant were cloned into a modified pCDNA4 vector with an N-terminal decahistidine tag fused in-frame with EGFP as described previously (53). This His$_{10}$-GFP-talin1 backbone vector was used to subclone full-length talin2 and its mutant to generate His$_{10}$-GFP-talin2 constructs. Similarly, a Neptune2.5 tag was subcloned in place of the GFP tag to produce Neptune2.5-tagged talin2 construct for co-expression experiment. The cytomegalovirus promoter–driven mCherry-CAAX constructs were used directly as described earlier (75). All clones were verified by in-house sequencing.

Protein preparation

Bacterial expression plasmids were transformed in the *Escherichia coli* strains BL21 (DE3) Rosetta2 (Novagen) or in BL21-CodonPlus (DE3)-RIL (Agilent Technology). Proteins were either expressed by autoinduction (55) or induced with 0.2 mM isopropyl β-D-1-thiogalactopyranoside at 30 °C. For purification of WT or mutant talin2, cell pellets were resuspended in 20 mM Tris-HCl (pH 7.5), 400 mM NaCl, and 10 mM imidazole, lysed by sonication, and clarified by ultracentrifugation (100,000 × *g* for 30 min). The clarified cell lysates were loaded onto a nickel affinity column (GE Healthcare), which was equilibrated with 20 mM Tris-HCl (pH 7.5), 400 mM NaCl, and 20 mM imidazole. Proteins were eluted using a 0.5 M imidazole gradient. The histidine tags were removed by overnight cleavage with PreScission protease at 4 °C and dialyzed into 20 mM Tris (pH 7.5), 400 mM NaCl, 2 mM DTT, and 1 mM EDTA. Proteins were further purified by size-exclusion chromatography using a Superdex 75 column (GE Healthcare) equilibrated with 20 mM Tris-HCl (pH 7.5), 400 mM NaCl, 2 mM DTT, and 0.1 mM EDTA. All proteins were concentrated, and aliquots were frozen in liquid nitrogen and stored at −20 °C. Full-length talin1, talin2, and talin rod domains were purified by nickel-affinity chromatography followed by size-exclusion chromatography on a Superose 6 10/300 column (GE Healthcare). For full-length proteins and the talin rod domains (residues 1–2,541, 437–2,541, 437–2,493 for talin1; 1–2,542 for talin2), the salt concentration was maintained at a physiological level of 150 mM.

Talin2 crystallization

Human talin2 (residues 1–403) was concentrated to 5–20 mg/ml. Crystals were grown by hanging drop vapor diffusion at room temperature using a protein/reservoir ratio of 1:1 from 100 mM HEPES (pH 7) and 8% (w/v) PEG 8,000. Hexagonal needle-shaped crystals formed within 2–3 days and continued to grow for a week. Crystals were transferred briefly to a drop containing the reservoir solution that included 25% glycerol as cryoprotectant and mounted with no preferred orientation and flash-frozen in liquid nitrogen. Diffraction-quality crystals were obtained from 100 mM HEPES (pH 7) and 8% (w/v) PEG 8,000.

Talin2 X-ray data collection and processing

Human talin2 (residues 1–403) crystals diffracted X-rays at beamline ID22 at the Advanced Photon Source at Argonne National Laboratory to ~2.6-Å Bragg spacings. The beamline was equipped with a Rayonix MX300-HS (MarCCD 300) detector, and a complete data set of 360 frames were collected at 1.0043 Å wavelength with a 0.5° oscillation range. X-ray data were indexed, integrated, and scaled using XDS and AIMLESS as implemented in autoPROC (76). Data reduction statistics are provided in Table 1.

Talin2 structure determination and crystallographic refinement

Phases were obtained by molecular replacement as implemented in the program PHASER (77) using the talin1 F0-F1 subdomain structure (PDB entry 6MFS) (55) and the talin2 F2-F3 subdomain structure (PDB entry 3G9W) (67) as search models. A unique solution was only obtained when both search models were used as ensembles in Phaser with one polypeptide chain in the asymmetric unit in space group $P\,6_5$, resulting in a calculated volume/mass ratio of 2.18 $Å^3$/Da, corresponding to a solvent content of ~0.436. A small fraction of the data (0.06) was identified as merohedrally twinned by Phenix Xtriage (78). Initial refinements without translation, libration, screw rotation (TLS) parameters or twinning operator were performed until convergence using autoBuster (79), and then manually built the model using Coot (80). Further model refinements were carried out by including 12 TLS groups and the twinning operator using Phenix. By taking the twinning operator into account, the *R*-factor gap was reduced from 10 to 5% using the $P\,6_5$ merohedral twinning operator. Also, part of the F1 insert residues 134–173 were unambiguously resolved after final refinement with Phenix, and the missing region was manually built using omit maps in Coot. However, a small part of the F1 insert, residues 143–153, were not built because of weak electron densities. The quality of the final model was assessed using MolProbity (81), which revealed no outliers, and the final crystallographic refinement statistics are provided in Table 2.

Lipid co-sedimentation assays

PIP_2 binding to WT and mutant talin proteins was assayed as described previously (82). Lipid vesicles of PC and PIP_2 were prepared in chloroform to a final composition of 80% PC and 20% PIP_2. The lipid mixture was dried under an argon stream until the dry lipid film attached to the glass vial bottom and then resuspended in 20 mM Tris (pH 7.5), 400 mM NaCl, and 2 mM 1,4-DTT (buffer A). Small unilamellar vesicles were then produced by sonication after incubating the lipid vesicles at 37 °C for 30 min. Samples containing 50 μg of total lipid in a 12-μl suspension and 50 μM proteins (WT or mutant) were incubated at 4 °C for 1 h followed by centrifugation at 100,000 × *g* for 30 min. Supernatants and pellets were separated, and the pellets were carefully washed with buffer A twice and then resuspended in 12 μl of SDS sample buffer. The supernatant and pellet samples were analyzed by SDS-PAGE.

Vesicle pull-down assays

Lipid vesicles were prepared by mixing dissolved phospholipids (Avanti Polar Lipids) to obtain 6% (mol/mol) PIP_2 in PC. The solvent was dried under an argon stream. Lipid films were resuspended in 20 mM Hepes (pH 7.5), 400 mM NaCl, 0.5 mM EDTA, 0.5 mM tris(2-carboxyethyl)phosphine (TCEP) and sonicated until resuspended. Vesicle pulldowns were performed with 2 μM talin1 (residues 1–400) or talin2 (residues 1–403) by serial dilution of the vesicles. After 2 h of incubation, the vesicles were centrifuged for 15 min at 16,100 × *g* at 4 °C. Supernatants were collected, and the pelleted vesicles were washed and resuspended. Protein pellets and supernatants were quantified by the Bradford method (Bio-Rad) at an absorption of 590 nm. For all samples, the buffer blanks were subtracted.

Multiangle light scattering (MALS)

SEC with MALS analyses were carried out on an Agilent 1260 Infinity HPLC system equipped with a variable wavelength detector for UV absorption monitoring coupled to a DAWN-HELEOS II multiangle light-scattering detector (Wyatt Technology) and OptiLab T-rex differential refractive index detector (Wyatt Technology). SEC was carried out at a flow rate of 0.5 ml/min in 20 mM Tris-HCl, pH 8, 400 mM NaCl, 0.5 mM EDTA, and 1 mM DTT buffer for the talin head domains and 20 mM Tris-HCl, pH 7.5, 150 mM NaCl, and 0.5 mM TCEP buffer for the full-length talin protein. BSA at 2 mg/ml was used as a standard, and ASTRA software version 6.1 was used to control the data acquisition and analysis to determine the molar mass of the protein.

Thermal shift analysis

The structural integrity of the mutant proteins was verified by thermal shift analyses to compare the denaturation profile with the WT protein and was carried out as reported earlier (83). Briefly, proteins were subjected to thermal melt analyses in a standard white opaque quantitative PCR plate in a total volume of 20 µl. The analyses were carried out in a buffer of 20 mM Tris-HCl, pH 7.5, 400 mM NaCl, and 1 mM DTT containing a 10 μM protein sample and 2.5-fold concentration of SYPRO Orange dye (Thermo Fisher Scientific). The Roche 480 thermocycler was used for measuring the denaturation profile using the predefined melting curve program with excitation at 483 nm and emission of 568 nm. Samples were allowed to equilibrate at 25 °C for 15 s prior to ramping the temperature to 90 °C at 0.1 °C/s with continuous monitoring of the change in fluorescence. All experiments were carried out twice. The averages of triplicate sample measurements from each experiment were plotted to obtain denaturation profiles, and the first derivative plot of change in fluorescence *versus* temperature was used to derive melting temperature, T_m.

Immunostaining and FLIM cell preparation

talin$^{-/-}$ papillary collecting duct cells (kindly provided by Roy Zent, University of Vanderbilt) were used for transient transfection and further analyses by FLIM and immunostaining. Cells were routinely cultured in Dulbecco's modified Eagle's medium F-12 (Thermo Fisher Scientific) supplemented with 10% fetal bovine serum, 100 µg/ml streptomycin, and 100 units/ml penicillin at 37 °C with 5% CO_2 in a humidified incubator. For live-cell imaging or confocal microscopy, full-length GFP-talin constructs were transiently co-transfected in papillary collecting duct cells along with mCherry fused at the C terminus by the K-Ras–derived CAAX domain (DGKKKKKKSKTKCVIM). Transfections were carried out in a 6-well plate using Lipofectamine 3000 (Lifesciences Inc.) as per the manufacturer's suggested protocol. Cells transfected with GFP-talin alone were used as a control. After transfections, cells were used to probe expression of GFP-talin constructs by immunoblotting using the anti-GFP antibody (Millipore Sigma), and the remaining cells were used either for live-cell imaging for FLIM analyses or for immunostaining. For the latter, 24 h post-transfection, cells were trypsinized and seeded on a 2-µg/ml fibronectin-coated coverslip at a cell density of 0.5×10^6 cells in a 24-well plate in a total of 0.5 ml of growth media. Cells were allowed to attach for 24 h and washed twice with PBS and subsequently fixed and permeabilized concurrently using 0.5% Triton X-100 and 4% paraformaldehyde for 5 min at 37 °C and 5% carbon dioxide (CO_2). After washing with PBS, cells were incubated for another 20 min at 37 °C and 5% CO_2 to aid proper cell fixation. Cells were washed three times with PBS, blocked with 1% BSA in PBS, and stained for actin with Alex Fluor 633 phalloidin in 1% BSA for 1 h. Subsequently, cells were washed twice with PBS and mounted with or without NucBlue^{TM}. Confocal images of the immunostained cells were recorded on an Abberior Instruments Expert-Line STED (stimulated emission depletion) nanoscope using the pulsed 485-, 561-, and 640-nm excitation laser lines in a line-interleaved fashion with the detection windows set between 500 and 550 nm for the green channel, between 610 and 630 nm for the red, and between 650 and 720 nm for the far-red channels. All images were acquired using a 100-fold, 1.4 numerical aperture oil immersion objective lens (Olympus), the QUAD beam scanner, and the Imspector software package (Max-Planck Innovation).

For the total cell area and focal adhesion measurements, confocal images were carried out on Zeiss LSM880 laser-scanning confocal microscope using either plan-apochromat ×20 (1.4 numerical aperture) or plan-apochromat ×63 (1.4 numerical aperture) oil differential interference contrast objectives. Excitation of the GFP fluorophore was achieved using the 488-nm laser, and the emission was recorded at 524 nm. Appropriate band pass filtering and threshold were applied to enable proper measurement of the total cell area and focal adhesions using the "Analyze particles" option in the Fiji (ImageJ) software (84). To eliminate the inclusion of measurement outliers (including, for example, multiple fused adhesions, thick cell periphery in minimally spread cells), focal adhesion areas that were more than 3 times the areas represented by the median were excluded from the analyses. For the mutants, this was much more difficult, as only some cells exhibited clear focal adhesions and the remaining cells had connecting features that falsely represented focal adhesions. Here, low band pass filtering was administered.

FLIM with FRET two-photon (2p) microscopy and 2p FLIM

To measure the talin association with the membrane, we performed 2p FLIM imaging using a custom 2p microscope (85). Briefly, GFP was excited with a Ti:sapphire laser (Chameleon, Coherent) at a wavelength of 920 nm and a power of 1.4-1.6 milliwatts measured below the objective. mCherry was excited by a 1,100-nm, 120-fs pulsed, 80-MHz two-photon INSIGHT laser (Spectra-Physics). The fluorescence was collected with an objective (×60, 1.0 numerical aperture, Olympus), divided with a dichroic mirror (565 nm), and detected with a low-transfer time spread photoelectron multiplier tube (H7422-40p from Hamamatsu) placed after a 510/70 2p wavelength filter (Chroma) for green fluorescence and a 620/90 2p wavelength filter (Chroma) to collect red fluorescence. Fluorescence lifetime images were acquired with two PCI-6110 cards (National Instruments) using a time-correlated single-photon counting board (Timeharp 260 P; PicoQuant) controlled with custom software written in C# (source code available at https://github.com/ryoheiyasuda/FLIMage_public).

FLIM analyses

The fluorescence lifetime decay curve *F(t)* from cells with similar expression levels of the talin sensor (number of photons less than 500,000 and donor/acceptor ratios between 0.5 and 4) was fit with a biexponential function convolved with the Gaussian pulse response function, $F(t) = F_0(P_D H(t, t_0, \tau_D, \tau_G) + P_{AD} H(t, t_0, \tau_{AD}, \tau_G))$, where τ_{AD} is fluorescence lifetime of the donor bound with acceptor, P_D and P_{AD} are the fraction of free donor and donor undergoing FRET with the acceptor, respectively, and $H(t)$ is an exponential function convolved with the Gaussian instrument response function $H(t, t_0, \tau_D, \tau_G) = \frac{1}{2}\exp\left(\frac{\tau_G^2}{2\tau_i^2} - \frac{t-t_0}{\tau_i}\right)\operatorname{erfc}\left(\frac{\tau_G^2 - \tau_i(t-t_0)}{2\tau_i\tau_G}\right)$ where τ_D is the fluorescence lifetime of the free donor, τ_G is the width of the Gaussian pulse response function, t_0 is the time offset, and erfc is the complementary error function. We obtained τ_D from single-exponential fits ($P_{AD} = 0$) to fluorescence lifetime curves of GFP-talin1 expressed in live cells (2.72 ns ± 0.01, $n = 14$) and GFP-talin2 (2.75 ns ± 0.008, $n = 8$) and estimated τ_{AD} (1.33 ns). For experimental data, we fixed τ_D and τ_{AD} to these values to obtain stable fitting. To generate a fluorescence lifetime image, we calculated the mean photon arrival time ($<t>$), in each pixel as $<t> = \int tF(t)\mathrm{d}t / \int F(t)\mathrm{d}t$. The mean photon arrival time is related to the mean fluorescence lifetime (τ_m) by an offset arrival time t_0, which is obtained by fitting the whole image to $\tau_m = <t> - t_o$. The binding fraction of talin (P_{AD}) was calculated from fitting.

Data availability

The coordinates were deposited with the Protein Data Bank, accession code 6U4K. All other data are contained within the article and the accompanying supporting information.

Acknowledgments—We are indebted to the staff of the South Eastern Regional Access Team (Argonne National Laboratory) for synchrotron support. talin$^{-/-}$ cells were a generous gift from Roy Zent (Vanderbilt School of Medicine). The human talin2 cDNA was a generous gift from Richard O. McCann (University of Kentucky). We thank Charmane Gabriel (Oxbridge Academy) for technical help, Nicolai Urban (Max Planck Florida Institute) for help with microscopes, and Peter Moody (Leicester University) and Katrin Karbstein (The Scripps Research Institute) for helpful structure and biochemistry insights, respectively.

Funding and additional information—T. I. is supported by grants from the National Institutes of Health, the Department of Defense, and the National Science Foundation and by start-up funds provided to The Scripps Research Institute from the State of Florida. This is publication 29850 from The Scripps Research Institute. The content is solely the responsibility of the authors and does not necessarily represent the official views of the National Institutes of Health.

Conflict of interest—R. Y. is a founder of Florida Lifetime Imaging LLC.

Abbreviations—The abbreviations used are: PIP$_2$, phosphatidylinositol 4,5-bisphosphate; FERM, four point one, ezrin, radixin, moesin; E, embryonic day; FLIM, fluorescence lifetime imaging; FRET, Förster/fluorescence resonance energy transfer; PDB, Protein Data Bank; PC, phosphatidylcholine; mEGFP, monomeric enhanced GFP; SAXS, small-angle X-ray scattering; TCEP, tris(2-carboxyethyl)phosphine; SEC, size-exclusion chromatography; MALS, multiangle light scattering; 2p, two-photon; LBD, lipid binding–deficient; TLS translation, libration, screw rotation.

References

1. Desiniotis, A., and Kyprianou, N. (2011) Significance of talin in cancer progression and metastasis. *Int. Rev. Cell Mol. Biol.* **289,** 117–147 CrossRef Medline
2. Huang, C., Rajfur, Z., Yousefi, N., Chen, Z., Jacobson, K., and Ginsberg, M. H. (2009) Talin phosphorylation by Cdk5 regulates Smurf1-mediated talin head ubiquitylation and cell migration. *Nat. Cell Biol.* **11,** 624–630 CrossRef Medline
3. Jin, J. K., Tien, P. C., Cheng, C. J., Song, J. H., Huang, C., Lin, S. H., and Gallick, G. E. (2015) Talin1 phosphorylation activates β1 integrins: a novel mechanism to promote prostate cancer bone metastasis. *Oncogene* **34,** 1811–1821 CrossRef Medline
4. Tadokoro, S., Shattil, S. J., Eto, K., Tai, V., Liddington, R. C., de Pereda, J. M., Ginsberg, M. H., and Calderwood, D. A. (2003) Talin binding to integrin β tails: a final common step in integrin activation. *Science* **302,** 103–106 CrossRef Medline
5. Calderwood, D. A., Zent, R., Grant, R., Rees, D. J., Hynes, R. O., and Ginsberg, M. H. (1999) The Talin head domain binds to integrin β subunit cytoplasmic tails and regulates integrin activation. *J. Biol. Chem.* **274,** 28071–28074 CrossRef Medline
6. Bate, N., Gingras, A. R., Bachir, A., Horwitz, R., Ye, F., Patel, B., Goult, B. T., and Critchley, D. R. (2012) Talin contains a C-terminal calpain2 cleavage site important in focal adhesion dynamics. *PLoS ONE* **7,** e34461 CrossRef Medline
7. Beaty, B. T., and Condeelis, J. (2014) Digging a little deeper: the stages of invadopodium formation and maturation. *Eur. J. Cell Biol.* **93,** 438–444 CrossRef Medline
8. Franco, S. J., Rodgers, M. A., Perrin, B. J., Han, J., Bennin, D. A., Critchley, D. R., and Huttenlocher, A. (2004) Calpain-mediated proteolysis of talin regulates adhesion dynamics. *Nat. Cell Biol.* **6,** 977–983 CrossRef Medline
9. Nayal, A., Webb, D. J., and Horwitz, A. F. (2004) Talin: an emerging focal point of adhesion dynamics. *Curr. Opin. Cell Biol.* **16,** 94–98 CrossRef Medline
10. Saykali, B. A., and El-Sibai, M. (2014) Invadopodia, regulation, and assembly in cancer cell invasion. *Cell Commun. Adhes.* **21,** 207–212 CrossRef Medline
11. Webb, D. J., Parsons, J. T., and Horwitz, A. F. (2002) Adhesion assembly, disassembly and turnover in migrating cells—over and over and over again. *Nat. Cell Biol.* **4,** E97–E100 CrossRef Medline
12. Wehrle-Haller, B. (2012) Assembly and disassembly of cell matrix adhesions. *Curr. Opin. Cell Biol.* **24,** 569–581 CrossRef Medline
13. Giannone, G., Jiang, G., Sutton, D. H., Critchley, D. R., and Sheetz, M. P. (2003) Talin1 is critical for force-dependent reinforcement of initial integrin-cytoskeleton bonds but not tyrosine kinase activation. *J. Cell Biol.* **163,** 409–419 CrossRef Medline
14. Zhang, X., Jiang, G., Cai, Y., Monkley, S. J., Critchley, D. R., and Sheetz, M. P. (2008) Talin depletion reveals independence of initial cell spreading from integrin activation and traction. *Nat. Cell Biol.* **10,** 1062–1068 CrossRef Medline
15. Chen, C., Wang, X., Xiong, X., Liu, Q., Huang, Y., Xu, Q., Hu, J., Ge, G., and Ling, K. (2015) Targeting type Iγ phosphatidylinositol phosphate kinase inhibits breast cancer metastasis. *Oncogene* **34,** 4635–4646 CrossRef Medline
16. Di Paolo, G., Pellegrini, L., Letinic, K., Cestra, G., Zoncu, R., Voronov, S., Chang, S., Guo, J., Wenk, M. R., and De Camilli, P. (2002) Recruitment and regulation of phosphatidylinositol phosphate kinase type 1γ by the FERM domain of talin. *Nature* **420,** 85–89 CrossRef Medline
17. Li, X., Zhou, Q., Sunkara, M., Kutys, M. L., Wu, Z., Rychahou, P., Morris, A. J., Zhu, H., Evers, B. M., and Huang, C. (2013) Ubiquitylation of

phosphatidylinositol 4-phosphate 5-kinase type Iγ by HECTD1 regulates focal adhesion dynamics and cell migration. *J. Cell Sci.* **126,** 2617–2628 CrossRef Medline

18. Ling, K., Doughman, R. L., Firestone, A. J., Bunce, M. W., and Anderson, R. A. (2002) Type Iγ phosphatidylinositol phosphate kinase targets and regulates focal adhesions. *Nature* **420,** 89–93 CrossRef Medline
19. Wu, J., Chen, Y., Lu, L. Y., Wu, Y., Paulsen, M. T., Ljungman, M., Ferguson, D. O., and Yu, X. (2011) Chfr and RNF8 synergistically regulate ATM activation. *Nat. Struct. Mol. Biol.* **18,** 761–768 CrossRef Medline
20. Goult, B. T., Xu, X. P., Gingras, A. R., Swift, M., Patel, B., Bate, N., Kopp, P. M., Barsukov, I. L., Critchley, D. R., Volkmann, N., and Hanein, D. (2013) Structural studies on full-length talin1 reveal a compact auto-inhibited dimer: implications for talin activation. *J. Struct. Biol.* **184,** 21–32 CrossRef Medline
21. Nuckolls, G. H., Turner, C. E., and Burridge, K. (1990) Functional studies of the domains of talin. *J. Cell Biol.* **110,** 1635–1644 CrossRef Medline
22. Bass, M. D., Patel, B., Barsukov, I. G., Fillingham, I. J., Mason, R., Smith, B. J., Bagshaw, C. R., and Critchley, D. R. (2002) Further characterization of the interaction between the cytoskeletal proteins talin and vinculin. *Biochem. J.* **362,** 761–768 CrossRef Medline
23. Bois, P. R., Borgon, R. A., Vonrhein, C., and Izard, T. (2005) Structural dynamics of α-actinin-vinculin interactions. *Mol. Cell Biol.* **25,** 6112–6122 CrossRef Medline
24. Fillingham, I., Gingras, A. R., Papagrigoriou, E., Patel, B., Emsley, J., Critchley, D. R., Roberts, G. C., and Barsukov, I. L. (2005) A vinculin binding domain from the talin rod unfolds to form a complex with the vinculin head. *Structure* **13,** 65–74 CrossRef Medline
25. Gingras, A. R., Vogel, K. P., Steinhoff, H. J., Ziegler, W. H., Patel, B., Emsley, J., Critchley, D. R., Roberts, G. C., and Barsukov, I. L. (2006) Structural and dynamic characterization of a vinculin binding site in the talin rod. *Biochemistry* **45,** 1805–1817 CrossRef Medline
26. Gingras, A. R., Ziegler, W. H., Frank, R., Barsukov, I. L., Roberts, G. C. K., Critchley, D. R., and Emsley, J. (2005) Mapping and consensus sequence identification for multiple vinculin binding sites within the talin rod. *J. Biol. Chem.* **280,** 37217–37224 CrossRef Medline
27. Izard, T., and Vonrhein, C. (2004) Structural basis for amplifying vinculin activation by talin. *J. Biol. Chem.* **279,** 27667–27678 CrossRef Medline
28. Papagrigoriou, E., Gingras, A. R., Barsukov, I. L., Bate, N., Fillingham, I. J., Patel, B., Frank, R., Ziegler, W. H., Roberts, G. C., Critchley, D. R., and Emsley, J. (2004) Activation of a vinculin-binding site in the talin rod involves rearrangement of a five-helix bundle. *EMBO J.* **23,** 2942–2951 CrossRef Medline
29. Tran Van Nhieu, G., and Izard, T. (2007) Vinculin binding in its closed conformation by a helix addition mechanism. *EMBO J.* **26,** 4588–4596 CrossRef Medline
30. Yogesha, S. D., Rangarajan, E. S., Vonrhein, C., Bricogne, G., and Izard, T. (2012) Crystal structure of vinculin in complex with vinculin binding site 50 (VBS50), the integrin binding site 2 (IBS2) of talin. *Protein Sci.* **21,** 583–588 CrossRef Medline
31. Yogesha, S. D., Sharff, A., Bricogne, G., and Izard, T. (2011) Intermolecular versus intramolecular interactions of the vinculin binding site 33 of talin. *Protein Sci.* **20,** 1471–1476 CrossRef Medline
32. Izard, T., Evans, G., Borgon, R. A., Rush, C. L., Bricogne, G., and Bois, P. R. (2004) Vinculin activation by talin through helical bundle conversion. *Nature* **427,** 171–175 CrossRef Medline
33. Atherton, P., Stutchbury, B., Wang, D. Y., Jethwa, D., Tsang, R., Meiler-Rodriguez, E., Wang, P., Bate, N., Zent, R., Barsukov, I. L., Goult, B. T., Critchley, D. R., and Ballestrem, C. (2015) Vinculin controls talin engagement with the actomyosin machinery. *Nat. Commun.* **6,** 10038 CrossRef Medline
34. Gingras, A. R., Bate, N., Goult, B. T., Hazelwood, L., Canestrelli, I., Grossmann, J. G., Liu, H., Putz, N. S., Roberts, G. C., Volkmann, N., Hanein, D., Barsukov, I. L., and Critchley, D. R. (2008) The structure of the C-terminal actin-binding domain of talin. *EMBO J.* **27,** 458–469 CrossRef Medline
35. Hemmings, L., Rees, D. J., Ohanian, V., Bolton, S. J., Gilmore, A. P., Patel, B., Priddle, H., Trevithick, J. E., Hynes, R. O., and Critchley, D. R. (1996) Talin contains three actin-binding sites each of which is adjacent to a vinculin-binding site. *J. Cell Sci.* **109,** 2715–2726 Medline
36. Smith, S. J., and McCann, R. O. (2007) A C-terminal dimerization motif is required for focal adhesion targeting of Talin1 and the interaction of the Talin1 I/LWEQ module with F-actin. *Biochemistry* **46,** 10886–10898 CrossRef Medline
37. Lee, H. S., Bellin, R. M., Walker, D. L., Patel, B., Powers, P., Liu, H., Garcia-Alvarez, B., de Pereda, J. M., Liddington, R. C., Volkmann, N., Hanein, D., Critchley, D. R., and Robson, R. M. (2004) Characterization of an actin-binding site within the talin FERM domain. *J. Mol. Biol.* **343,** 771–784 CrossRef Medline
38. Monkley, S. J., Pritchard, C. A., and Critchley, D. R. (2001) Analysis of the mammalian talin2 gene TLN2. *Biochem. Biophys. Res. Commun.* **286,** 880–885 CrossRef Medline
39. Thul, P. J., Akesson, L., Wiking, M., Mahdessian, D., Geladaki, A., Ait Blal, H., Alm, T., Asplund, A., Björk, L., Breckels, L. M., Bäckstrom, A., Danielsson, F., Fagerberg, L., Fall, J., Gatto, L., *et al.* (2017) A subcellular map of the human proteome. *Science* **356,** eaal3321 CrossRef Medline
40. Praekelt, U., Kopp, P. M., Rehm, K., Linder, S., Bate, N., Patel, B., Debrand, E., Manso, A. M., Ross, R. S., Conti, F., Zhang, M. Z., Harris, R. C., Zent, R., Critchley, D. R., and Monkley, S. J. (2012) New isoform-specific monoclonal antibodies reveal different sub-cellular localisations for talin1 and talin2. *Eur. J. Cell Biol.* **91,** 180–191 CrossRef Medline
41. Senetar, M. A., Moncman, C. L., and McCann, R. O. (2007) Talin2 is induced during striated muscle differentiation and is targeted to stable adhesion complexes in mature muscle. *Cell Motil. Cytoskeleton* **64,** 157–173 CrossRef Medline
42. Monkley, S. J., Zhou, X.-H., Kinston, S. J., Giblett, S. M., Hemmings, L., Priddle, H., Brown, J. E., Pritchard, C. A., Critchley, D. R., and Fässler, R. (2000) Disruption of the talin gene arrests mouse development at the gastrulation stage. *Dev. Dyn.* **219,** 560–574 CrossRef Medline
43. Conti, F. J., Monkley, S. J., Wood, M. R., Critchley, D. R., and Muller, U. (2009) Talin 1 and 2 are required for myoblast fusion, sarcomere assembly and the maintenance of myotendinous junctions. *Development* **136,** 3597–3606 CrossRef Medline
44. Conti, F. J., Felder, A., Monkley, S., Schwander, M., Wood, M. R., Lieber, R., Critchley, D., and Müller, U. (2008) Progressive myopathy and defects in the maintenance of myotendinous junctions in mice that lack talin 1 in skeletal muscle. *Development* **135,** 2043–2053 CrossRef Medline
45. Austen, K., Ringer, P., Mehlich, A., Chrostek-Grashoff, A., Kluger, C., Klingner, C., Sabass, B., Zent, R., Rief, M., and Grashoff, C. (2015) Extracellular rigidity sensing by talin isoform-specific mechanical linkages. *Nat. Cell Biol.* **17,** 1597–1606 CrossRef Medline
46. Manso, A. M., Okada, H., Sakamoto, F. M., Moreno, E., Monkley, S. J., Li, R., Critchley, D. R., and Ross, R. S. (2017) Loss of mouse cardiomyocyte talin-1 and talin-2 leads to β-1 integrin reduction, costameric instability, and dilated cardiomyopathy. *Proc. Natl. Acad. Sci. U. S. A.* **114,** E6250–E6259 CrossRef Medline
47. Le, X. F., Almeida, M. I., Mao, W., Spizzo, R., Rossi, S., Nicoloso, M. S., Zhang, S., Wu, Y., Calin, G. A., and Bast, R. C., Jr. (2012) Modulation of microRNA-194 and cell migration by HER2-targeting trastuzumab in breast cancer. *PLoS ONE* **7,** e41170 CrossRef Medline
48. Soe, Z. Y., Prajuabjinda, O., Myint, P. K., Gaowa, A., Kawamoto, E., Park, E. J., and Shimaoka, M. (2019) Talin-2 regulates integrin functions in exosomes. *Biochem. Biophys. Res. Commun.* **512,** 429–434 CrossRef Medline
49. Dedden, D., Schumacher, S., Kelley, C. F., Zacharias, M., Biertumpfel, C., Fassler, R., and Mizuno, N. (2019) The architecture of Talin1 reveals an autoinhibition mechanism. *Cell* **179,** 120–131.e13 CrossRef Medline
50. Elliott, P. R., Goult, B. T., Kopp, P. M., Bate, N., Grossmann, J. G., Roberts, G. C., Critchley, D. R., and Barsukov, I. L. (2010) The structure of the talin head reveals a novel extended conformation of the FERM domain. *Structure* **18,** 1289–1299 CrossRef Medline
51. Campbell, I. D. (2010) The talin FERM domain is not so FERM. *Structure* **18,** 1222–1223 CrossRef Medline
52. Li, H., Deng, Y., Sun, K., Yang, H., Liu, J., Wang, M., Zhang, Z., Lin, J., Wu, C., Wei, Z., and Yu, C. (2017) Structural basis of kindlin-mediated integrin recognition and activation. *Proc. Natl. Acad. Sci. U. S. A.* **114,** 9349–9354 CrossRef Medline
53. Chinthalapudi, K., Mandati, V., Zheng, J., Sharff, A. J., Bricogne, G., Griffin, P. R., Kissil, J., and Izard, T. (2018) Lipid binding promotes the open

conformation and tumor-suppressive activity of neurofibromin 2. *Nat. Commun.* **9,** 1338 CrossRef Medline

54. Goult, B. T., Bouaouina, M., Elliott, P. R., Bate, N., Patel, B., Gingras, A. R., Grossmann, J. G., Roberts, G. C., Calderwood, D. A., Critchley, D. R., and Barsukov, I. L. (2010) Structure of a double ubiquitin-like domain in the talin head: a role in integrin activation. *EMBO J.* **29,** 1069–1080 CrossRef Medline
55. Chinthalapudi, K., Rangarajan, E. S., and Izard, T. (2018) The interaction of talin with the cell membrane is essential for integrin activation and focal adhesion formation. *Proc. Natl. Acad. Sci. U. S. A.* **115,** 10339–10344 CrossRef Medline
56. Goksoy, E., Ma, Y. Q., Wang, X., Kong, X., Perera, D., Plow, E. F., and Qin, J. (2008) Structural basis for the autoinhibition of talin in regulating integrin activation. *Mol. Cell* **31,** 124–133 CrossRef Medline
57. Song, X., Yang, J., Hirbawi, J., Ye, S., Perera, H. D., Goksoy, E., Dwivedi, P., Plow, E. F., Zhang, R., and Qin, J. (2012) A novel membrane-dependent on/off switch mechanism of talin FERM domain at sites of cell adhesion. *Cell Res.* **22,** 1533–1545 CrossRef Medline
58. Moore, D. T., Nygren, P., Jo, H., Boesze-Battaglia, K., Bennett, J. S., and DeGrado, W. F. (2012) Affinity of talin-1 for the beta3-integrin cytosolic domain is modulated by its phospholipid bilayer environment. *Proc. Natl. Acad. Sci. U. S. A.* **109,** 793–798 CrossRef Medline
59. Ye, X., McLean, M. A., and Sligar, S. G. (2016) Phosphatidylinositol 4,5-bisphosphate modulates the affinity of Talin-1 for phospholipid bilayers and activates its autoinhibited form. *Biochemistry* **55,** 5038–5048 CrossRef Medline
60. Goult, B. T., Bate, N., Anthis, N. J., Wegener, K. L., Gingras, A. R., Patel, B., Barsukov, I. L., Campbell, I. D., Roberts, G. C., and Critchley, D. R. (2009) The structure of an interdomain complex that regulates talin activity. *J. Biol. Chem.* **284,** 15097–15106 CrossRef Medline
61. Yasuda, R. (2006) Imaging spatiotemporal dynamics of neuronal signaling using fluorescence resonance energy transfer and fluorescence lifetime imaging microscopy. *Curr. Opin. Neurobiol.* **16,** 551–561 CrossRef Medline
62. Goni, G. M., Epifano, C., Boskovic, J., Camacho-Artacho, M., Zhou, J., Bronowska, A., Martin, M. T., Eck, M. J., Kremer, L., Grater, F., Gervasio, F. L., Perez-Moreno, M., and Lietha, D. (2014) Phosphatidylinositol 4,5-bisphosphate triggers activation of focal adhesion kinase by inducing clustering and conformational changes. *Proc. Natl. Acad. Sci. U. S. A.* **111,** E3177–E3186 CrossRef Medline
63. Klapholz, B., and Brown, N. H. (2017) Talin—the master of integrin adhesions. *J. Cell Sci.* **130,** 2435–2446 CrossRef Medline
64. Haining, A. W., Lieberthal, T. J., and Del Rio Hernández, H. (2016) Talin: a mechanosensitive molecule in health and disease. *FASEB J.* **30,** 2073–2085 CrossRef Medline
65. Burridge, K., and Connell, L. (1983) Talin: a cytoskeletal component concentrated in adhesion plaques and other sites of actin-membrane interaction. *Cell Motil.* **3,** 405–417 CrossRef Medline
66. Debrand, E., El Jai, Y., Spence, L., Bate, N., Praekelt, U., Pritchard, C. A., Monkley, S. J., and Critchley, D. R. (2009) Talin 2 is a large and complex gene encoding multiple transcripts and protein isoforms. *FEBS J.* **276,** 1610–1628 CrossRef Medline
67. Anthis, N. J., Wegener, K. L., Ye, F., Kim, C., Goult, B. T., Lowe, E. D., Vakonakis, I., Bate, N., Critchley, D. R., Ginsberg, M. H., and Campbell, I. D. (2009) The structure of an integrin/talin complex reveals the basis of inside-out signal transduction. *EMBO J.* **28,** 3623–3632 CrossRef Medline
68. Wegener, K. L., Partridge, A. W., Han, J., Pickford, A. R., Liddington, R. C., Ginsberg, M. H., and Campbell, I. D. (2007) Structural basis of integrin activation by talin. *Cell* **128,** 171–182 CrossRef Medline
69. Gingras, A. R., Bate, N., Goult, B. T., Patel, B., Kopp, P. M., Emsley, J., Barsukov, I. L., Roberts, G. C., and Critchley, D. R. (2010) Central region of talin has a unique fold that binds vinculin and actin. *J. Biol. Chem.* **285,** 29577–29587 CrossRef Medline
70. Gingras, A. R., Ziegler, W. H., Bobkov, A. A., Joyce, M. G., Fasci, D., Himmel, M., Rothemund, S., Ritter, A., Grossmann, J. G., Patel, B., Bate, N., Goult, B. T., Emsley, J., Barsukov, I. L., Roberts, G. C., *et al.* (2009) Structural determinants of integrin binding to the talin rod. *J. Biol. Chem.* **284,** 8866–8876 CrossRef Medline
71. Goult, B. T., Gingras, A. R., Bate, N., Barsukov, I. L., Critchley, D. R., and Roberts, G. C. (2010) The domain structure of talin: residues 1815-1973 form a five-helix bundle containing a cryptic vinculin-binding site. *FEBS Lett.* **584,** 2237–2241 CrossRef Medline
72. Molony, L., McCaslin, D., Abernethy, J., Paschal, B., and Burridge, K. (1987) Properties of talin from chicken gizzard smooth muscle. *J. Biol. Chem.* **262,** 7790–7795 Medline
73. Bussell, K. (2002) Destination lipid rafts. *Nat. Rev. Mol. Cell Biol.* **3,** 399–399 CrossRef
74. Chang, Y. C., Zhang, H., Franco-Barraza, J., Brennan, M. L., Patel, T., Cukierman, E., and Wu, J. (2014) Structural and mechanistic insights into the recruitment of talin by RIAM in integrin signaling. *Structure* **22,** 1810–1820 CrossRef Medline
75. Colgan, L. A., Hu, M., Misler, J. A., Parra-Bueno, P., Moran, C. M., Leitges, M., and Yasuda, R. (2018) PKCα integrates spatiotemporally distinct Ca^{2+} and autocrine BDNF signaling to facilitate synaptic plasticity. *Nat. Neurosci.* **21,** 1027–1037 CrossRef Medline
76. Vonrhein, C., and Bricogne, G. (2008) AutoPROC—a framework for automated data processing. *Acta Crystallogr. Sect. F Struct. Biol. Cryst. Commun.* **64,** C78
77. McCoy, A. J., Grosse-Kunstleve, R. W., Adams, P. D., Winn, M. D., Storoni, L. C., and Read, R. J. (2007) Phaser crystallographic software. *J. Appl. Crystallogr.* **40,** 658–674 CrossRef Medline
78. Adams, P. D., Afonine, P. V., Bunkóczi, G., Chen, V. B., Davis, I. W., Echols, N., Headd, J. J., Hung, L. W., Kapral, G. J., Grosse-Kunstleve, R. W., McCoy, A. J., Moriarty, N. W., Oeffner, R., Read, R. J., Richardson, D. C., *et al.* (2010) PHENIX: a comprehensive Python-based system for macromolecular structure solution. *Acta Crystallogr. D Biol. Crystallogr.* **66,** 213–221 CrossRef Medline
79. Bricogne, G., Blanc, E., Brandl, M., Flensburg, C., Keller, P., Paciorek, P., Roversi, P., Sharff, A., Smart, O. S., Vonrhein, C., and Womack, T. O. (2011) BUSTER version 2.9, Global Phasing Ltd., Cambridge, UK
80. Emsley, P., and Cowtan, K. (2004) Coot: model-building tools for molecular graphics. *Acta Crystallogr. D Biol. Crystallogr.* **60,** 2126–2132 CrossRef Medline
81. Davis, I. W., Murray, L. W., Richardson, J. S., and Richardson, D. C. (2004) MOLPROBITY: structure validation and all-atom contact analysis for nucleic acids and their complexes. *Nucleic Acids Res.* **32,** W615–W619 CrossRef Medline
82. Chinthalapudi, K., Rangarajan, E. S., Brown, D. T., and Izard, T. (2016) Differential lipid binding of vinculin isoforms promotes quasi-equivalent dimerization. *Proc. Natl. Acad. Sci. U. S. A.* **113,** 9539–9544 CrossRef Medline
83. Rangarajan, E. S., Lee, J. H., Yogesha, S. D., and Izard, T. (2010) A helix replacement mechanism directs metavinculin functions. *PLoS ONE* **5,** e10679 CrossRef Medline
84. Schindelin, J., Arganda-Carreras, I., Frise, E., Kaynig, V., Longair, M., Pietzsch, T., Preibisch, S., Rueden, C., Saalfeld, S., Schmid, B., Tinevez, J. Y., White, D. J., Hartenstein, V., Eliceiri, K., Tomancak, P., *et al.* (2012) Fiji: an open-source platform for biological-image analysis. *Nat Methods* **9,** 676–682 CrossRef Medline
85. Murakoshi, H., Wang, H., and Yasuda, R. (2011) Local, persistent activation of Rho GTPases during plasticity of single dendritic spines. *Nature* **472,** 100–104 CrossRef Medline